BrachyShade: Real-time Quality Assurance for High Dose Rate Brachytherapy

by

Roumani Alabd

A dissertation submitted in fulfilment of the requirements for the degree
Master of Engineering by Research

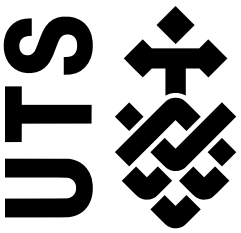

School of Electrical and Data Engineering
Faculty of Engineering and Information Technology
University of Technology Sydney

May 2018

Certificate of Original Authorship

I, Roumani Alabd, declare that this thesis titled, BrachyShade: Real-time Quality Assurance for High Dose Rate Brachytherapy, and the work presented in it is my own. I confirm that:

- This work was done wholly or mainly while in candidature for a research degree at this University.
- Where any part of this thesis has been previously submitted for a degree or any other qualification at this University or any other institution, this has been clearly stated.
- Where I have consulted the published work of others, this is always clearly attributed.
- Where I have quoted from the work of others, the source is always given. With the exception of such quotations, this thesis is entirely my own work.
- I have acknowledged all main sources of help.
- Where the thesis is based on work done by myself jointly with others, I have made clear exactly what was done by others and what I have contributed myself.

Production Note:
Signature removed
prior to publication.

May 2018
Roumani Alabd

Acknowledgements

I would first like to thank my thesis advisor Dr Daniel Franklin of the School of Electrical and Data Engineering at University of Technology Sydney. The door to Dr Franklin office was always open whenever I ran into a spot of troubles or had a question about my research or writing. He consistently allowed this paper to be my own work, but steered me in the right direction whenever he thought I needed it. This thesis would not be possible without his consistent and illuminating instructions.

I would also like to acknowledge Dave Hughes of the Climate Change Cluster (C3), Science Faculty at University of Technology Sydney as the second reader of a big portion of this thesis, and I am gratefully indebted to him for his very valuable comments on this work.

Finally, I must express my very profound gratitude to my parents and to my family for providing me with unfailing support and continuous encouragement throughout my years of study and through the process of researching and writing this thesis. This accomplishment would not have been possible without them. Thank you.

Dedication

To My Father

Abstract

High dose rate (HDR) brachytherapy is a popular form of radiotherapy in which radiation is delivered to the tumour via a small sealed radioactive source, which is moved through a sequence of positions in an array of catheters pre-implanted in the target area. Brachytherapy offers a key advantage over external beam radiotherapy, since the radiation dose is delivered directly to the diseased tissue while minimising the dose applied to healthy tissue in proximity to the target volume.

The accuracy of source placement is critical to the success of HDR brachytherapy. Deviations between the planned source position and the actual position achieved during treatment, due to anatomical changes (e.g. due to swelling or post-imaging tumour growth) or imperfect catheter placement, can harm healthy tissue or under-irradiate diseased tissue. Therefore, a reliable, accurate, real-time 3D source tracking system would be extremely valuable for treatment quality assurance and would allow a treatment plan to be modified in real time if positioning errors are detected.

HDR BrachyView is an in-body source tracking system designed to monitor the location of a HDR prostate brachytherapy source developed at the Centre of Medical Radiation Physics at the University of Wollongong, based on a tungsten pinhole camera with a silicon pixellated photon detector. Source position is estimated by back-projecting images of the source projected through the pinholes onto the imaging plane. Although HDR BrachyView has been shown to perform very well, it is challenging to manufacture, and suffers from a small systemic error in position estimation.

BrachyShade proposes to replace the tungsten collimator with a series of small spherical or spheroidal tungsten occluders embedded in a plastic shell, suspended over

the same pixellated detector (TimePix) used in the original HDR BrachyView. Instead of tracking bright projections of the source, the shadow of the source will be tracked, and by parametrically fitting an analytic model of the shadow map (where the model parameters are source position and intensity), the source position will be estimated. The proposed design significantly simplifies the manufacturing process, lowering the costs of manufacturing; it will also allow many more photons to arrive at the detector, enabling faster acquisition of a high quality position estimate. The achievable accuracy is comparable to HDR BrachyView, with a wider field of view achievable, depending on the specific configuration of tungsten occluders.

This Thesis presents a set of Monte Carlo simulations of the system, performed in Geant4. A sophisticated analytic model of the shadow map has been derived, and an algorithm developed which estimates the source position by minimising the error between the output of the analytic model and the detected photon map. A post-processing stage eliminates the effects of Compton scatter, which are otherwise mathematically challenging to include in the analytic model. Exhaustive test results proving the accuracy of the algorithm are presented. A second analytic method for estimating source position via a hierarchical pattern-matching strategy is also described, and preliminary results presented.

Keywords: Cancer, HDR Brachytherapy, Quality Assurance

Abbreviations

AAPM	American Association of Physicists in Medicine
ABS	American Brachytheapy Society
ACIM	Australian Cancer Incidence and Mortality workbooks
AIHW	Australian Institute of health and Welfare
AJCC	American Joint Committee on Cancer
BSDF	Backscatter dose fraction
BT	Brachytherapy
CCD	Charge-coupled device
CIRS	Computerized Imaging Reference Systems
CMRP	Centre for Medical Radiation Physics
CoG	Geometrical centre
CoMi	Ideal centre of mass
CRT	Conformal radiation therapy
CTV	Clinical Target Volume
DHT	Dihydrotestosterone
DRE	Digital rectal examination
DSP	Direct source projection
DVH	Dose Volume Histogram
D90	The Dose Delivered to at least 90% of The Target Volume
D80	The Dose Delivered to at least 80% of The Target Volume
EBRT	External Beam Radiotherapy
ESP	Extensive source projection

ESTRO	The European Society for Radiotherapy and Oncology
FOV	Field of View
HDR	High Dose Rate
IAEA	International Atomic Energy Agency
IEEE	Institute of Electrical and Electronics Engineers
IGRT	Image-guided radiation therapy
IMRT	Intensity modulated radiation therapy
ISUP	International Society of Urological Pathology
LDR	Low Dose Rate
LET	Linear energy transfer
MOSFET	Metal Oxide Semiconductor Field Effect
PBT	Prostate Brachytherapy
PCB	Printed Circuit Board
PDR	pulsed Dose Rate
PSD	Plastic Scintillation Detector
PTV	Planning Target Volume
OARs	Organs at Risks
QA	Quality Assurance
SD	Standard deviation
SBR	Signal to background ratio
SDD	Source to detector distance
SEM	Error of the sample mean
SNR	Signal to Noise Ratio
SSIM	Structural Similarity Index
SVD	Singular Value Decomposition
TLD	Thermoluminescent Dosimeters
ToA	Time of arrival mode
ToT	Time over threshold mode
TPS	Treatment Planning System
TRUS	Transrectal Ultrasound
V100	The Percentage of the Prostate Receiving %100 of the prescriped Dose
WED	Water-equivalent depth

Table of contents

List of figures

List of tables

CHAPTER 1

Introduction

After heart disease, cancer is the second most common cause of deaths in humans in 2017 [1]. One of the great advances in medicine in the past century has been the progress in developing new and ever-more effective treatments for cancer, while learning how to control the undesirable side-effects of these treatments. Radiotherapy is one of the key treatments for cancer, exploiting the differential between the impaired DNA-repair capabilities of malignant cells relative to normal tissue. A dose of radiation is delivered to the target area (which will result in some non-cancerous tissues being irradiated as well), either from a source outside the body, such as a linear accelerator (external beam radiation therapy), or from a radioactive source placed in the body either temporarily or permanently inside or in close proximity to the cancerous region (internal radiation therapy, known as *brachytherapy*, from the Greek word for 'short distance'). Currently, most radiotherapy utilises photon radiation such as X-rays or gamma rays. The amount of deposited radiation applied is adjusted depending on the type and stage of cancer being treated; for example, in curative cases, the dose for a solid epithelial tumour ranges from 60 to 80 Gy, while the applied radiation in lymphomas ranges from 20 to 40 Gy [2, 3]. Treatment planning software is used to determine the appropriate configuration of external radiation beams or the placement of radioactive source(s) that will deliver the therapeutic dose to the tumour while limiting radiation damage to radiosensitive healthy tissues.

Brachytherapy can be used to treat many types of cancer, but its greatest success to date has been in treating prostate cancer [4, 5]. Prostate cancer is the most commonly diagnosed cancers (after non-melanoma skin cancer) and one of the leading causes of cancer death among males in Australia and worldwide [6]. In 2017, it is estimated that there will be 16,665 new cases of prostate cancer and 3,452 deaths in Australia; in the United States, the respective figures are 161,360 and 26,730 [7–10]. The burden of disease (BoD) in Australia is significant, with many survivors suffering long-term physiological impairment as a result of their treatment, ranging from sexual dysfunction, incontinence and chronic pain to serious late complications such as radiotherapy-induced cancers. As the number of patients is so large, even a small improvement in current treatment methodologies - either in terms of efficacy of treatment or mitigation of side effects - is valuable, and has the potential to offer improved length and quality of life to many people.

The two main variants of brachytherapy used for treating prostate cancer are high dose rate (HDR) brachytherapy, which moves a single high-activity radiation source through the treatment volume; and low dose rate (LDR) brachytherapy, which involves permanent implantation of multiple small seeds containing a short-lived radioisotope. Of the two methods, HDR brachytherapy offers somewhat greater flexibility as the dwell time in each position can be precisely controlled to deliver a very specific dose to the tumour. While both LDR and HDR brachytherapy are currently in widespread clinical use, the work described in this Thesis specifically relates to HDR brachytherapy, with a particular focus on the prostate as the primary use case.

1.1 Prostate Brachytherapy and the Need for Real-Time Quality Assurance

In HDR prostate brachytherapy (HDR PBT), a small sealed capsule containing a high-activity radioactive source (typically ^{192}Ir or ^{60}Co) traverses the treatment volume via an array of plastic catheters which have been pre-implanted into the target region. The radioactive source is stepped through a sequence of positions in the catheters by a robotic afterloader, delivering the specified radiation dose distribution throughout the target volume according to the treatment plan. The accuracy of source placement is critical to the success of HDR brachytherapy treatment, where the objective is to conformally deliver the prescribed radiation dose to the target volume while limiting

the incidental dose delivered to surrounding radiation-sensitive healthy organs and tissues - in particular, the rectal wall, which is highly radiosensitive.

Deviations between the planned source position and the actual positions achieved during treatment can occur due to anatomical changes (e.g. due to intra-treatment swelling or involuntary bowel or bladder movement) or imperfect catheter placement. These deviations will result in an error in the dose delivered to the target volume, potentially harming healthy tissue or under-irradiating diseased tissue. Therefore, a reliable, accurate, real-time 3D source tracking capability would be valuable for treatment quality assurance; it could also potentially adjust a treatment plan in real time if positioning discrepancies are detected.

Several previous systems have been developed for source tracking during HDR prostate brachytherapy, as detailed in Chapter 2. However, as yet the only design which offers true real-time 3D source tracking capabilities is HDR BrachyView, developed by the University of Wollongong's Centre for Medical Radiation Physics. This device is essentially an in-body pinhole camera with an integrated trans-rectal ultrasound (TRUS) probe. The camera combines a multi-double-cone pinhole tungsten collimator with a high-resolution pixellated silicon photodetector array, and the projected images of the source are analysed to estimate the source position. While this device effectively solves the problem of real-time source tracking for HDR prostate brachytherapy, the collimator is challenging to manufacture, and the device must be rotated in situ in order to cover the entire volume.

1.2 Objectives and Overview

This work proposes a source tracking system, *HDR BrachyShade*, which is inspired by HDR BrachyView, but which takes a very different approach to source tracking. The key idea is to use shadows of spherical tungsten occluders rather than projections through pinholes in a tungsten collimator as the means of determining the source position. This approach offers several advantages over the original design:

- High-precision spherical tungsten or tungsten alloy ball bearings are a low-cost commodity item already in widespread industrial use, and the remainder of the probe may be fabricated from any medical-grade polymer - or even 3D printed - with great precision. This avoids the problem accurately machining off-centre holes in a hard tungsten cylinder, which is necessary in HDR BrachyView due to the unavoidable asymmetry of the detector PCB;

- Higher photon flux reaches the detector surface compared to the original BrachyView design; therefore, high-quality images may be acquired at a higher frame rate than is possible with the original design;
- Unlike a double-cone pinhole in a cylindrical-shell collimator, a spherical occluder is entirely orientation-agnostic; it presents the same view to the source regardless of its relative orientation. This makes the derivation of a good analytic approximation of the relation between source position, occluder location and detected image quite straightforward. Using this analytic model, the source position may be estimated using an iterative error-minimisation algorithm, together with an empirical model of the effects of Compton scattering within the medium;
- Finally, the orientation-agnosticism of the spherical occluders mean that additional occluders may be added on either side of the central axis. This greatly expands the field of view of the detector, allowing the entire prostate volume to be monitored without the need to mechanically rotate the probe. Furthermore, with a 3D-printed plastic shell and spherical occluders, it is feasible to design a probe which allows the occluders to be repositioned as required (either by printing a new shell, or by snapping the occluders into alternative sockets in a single shell) to achieve optimal source tracking for an individual patient.

Exhaustive simulation studies have confirmed the properties of the proposed design and source tracking methodology; the probe's accuracy compares favourably to the results previously published for HDR BrachyView.

1.3 Summary of Contributions and Structure of this Thesis

1.3.1 Summary of Contributions

This work has resulted in the following outcomes:

- One major journal paper, with the same title as this thesis ("BrachyShade: Real-time Quality Assurance for High Dose Rate Brachytherapy"); this has been submitted for consideration in *IEEE Transactions on Biomedical Engineering*, and comprises the following major contributions:

  - An analytical method for source localisation based on analysis of the captured image, utilising a simplified analytical model of the system and a non-linear optimisation algorithm, implemented in MATLAB;
  - A generalised simulation framework built in Geant4 (C++) for simulating an arbitrary radiation source (with configurable activity, geometry and spectrum) above a detector with arbitrarily positioned spherical or ellipsoidal tungsten occluders (with adjustable geometry);
  - Exhaustive evaluation of the proposed methods in a simulated prostate radiotherapy scenario, in terms of positioning error, necessary acquisition time and other critical parameters, including the development of a general error-evaluation framework;

- Design of the next phase of simulation and experimental work, with two further papers: one conference paper, to be submitted to IEEE Engineering in Medicine and Biology Conference 2018, which will present initial experimental results obtained with a Timepix detector and prototype occluder array, and one journal paper, presenting a second localisation method (based on a hierarchical search of a five-dimensional look-up table) and a comparison with the position estimation algorithm described in the first journal paper).

1.3.2 Thesis Structure

The thesis is divided into the following chapters:

- Chapter 2 presents an extensive literature review of the principles of source tracking and the current techniques and devices used for source tracking or dosimetry validation in HDR brachytherapy;
- Chapter 3 describes the design of the probe, and the position estimation and Compton scatter correction algorithms, and describes simulations conducted to evaluate the accuracy of the source tracking method, and the different proposed geometries of the probe;
- Chapter 4 presents the results of this simulation study, including an evaluation of the efficacy of the Compton scatter correction method, discusses the implications of the results and compares the results to experimental results published for HDR BrachyView; and

- Chapter 5 concludes the work and discusses the next steps in the development of this design, including the first planned prototype and plans for preclinical evaluation.

CHAPTER 2

Literature Review

The application of ionising radiation and radioactive substances in the field of medicine has progressively expanded since the discovery of radium in the past century, in particular to provide an effective and reliable treatment of cancer. The basic principle of radiation therapy or *radiotherapy* is to apply radiation to a tumour's cells, damaging them to the point that they cease to be viable and progressively die [11, 12]. The applied radiation damages the DNA (the molecules inside the cells that carry genetic information and pass it from one generation to the next) and the mitochondria (the energy-generating organelles) inside the tumour cells, killing them and potentially triggering the deaths of neighbouring cells via indirect chemical signalling. Radiation therapy works because a radiation dose that can be tolerated by healthy tissues due to the error-correcting DNA repair mechanisms in normal cells may cause damage which is not repairable in the already-defective DNA of a cancer cell. Many types of cancer cell are substantially more radiosensitive than normal tissue, and a dose threshold exists at which cancer cells will die while normal cells survive unscathed.

Therapeutic radiation therapy may be produced by a machine outside the body, in which case it is known as *teletherapy* or external beam radiation therapy (EBRT). The radiation in EBRT is most commonly produced using an accelerator source such as a linear accelerator (linac), which produces either X-rays or electron beams, or a synchrotron, which can deliver photon, proton or heavy ion beams; formerly, a collimated radioactive source such as ^{60}Co would have been used to produce a beam

of gamma rays. Alternatively, therapeutic radiation can be emitted from radioactive sources placed in the body in close proximity to cancer cells. This is known as internal radiation therapy, and is commonly called *brachytherapy* (from the Greek word *brachy*, meaning short distance).

The radiation dose deposited in the target varies depending on the type and stage of cancer being treated. For example, in curative cases, the exact dose for a solid epithelial tumour ranges from 60 to 80 Gy, while the radiation dose applied in the treatment of lymphomas ranges from 20 to 40 Gy[4, 13]. The dose may be temporally fractionated, giving healthy tissues more of an opportunity to repair radiation-induced damage, while accumulating progressively greater amounts of damage to cancerous tissues. The prescribed doses can be delivered in a single fraction or over multiple fractions with various fractions schedules [2, 3].

2.1 Brachytherapy

Brachytherapy is a popular form of radiotherapy treatment, which is well-suited for the ablation of certain classes of malignant tumour. It is a form of radiotherapy in which radiation is delivered to the tumour via small sealed capsules containing radioactive material, which are placed within the target volume using an array of catheters - either temporarily or permanently. Brachytherapy is an effective treatment option in cases where the tumour is favourably positioned and compact.

Brachytherapy has been successfully used as a treatment for head, neck, brain, prostate, lung, cervical, and endometrial cancers, and has recently emerged as a treatment option for skin cancer [14]. Edmundson et al. describe a technique for breast brachytherapy, *MammoSite* which has been shown to be able to successfully treat early-stage breast cancer [15]. Hoskin et al., and Skowronek et al. state that using brachytherapy as a treatment for localised prostate cancer provides a significant advantage over the traditional external beam radiotherapy, resulting in improved precision of dose delivery and avoiding issues associated with organ movement which complicate the external beam approaches [4, 5]. In addition, Skowronek argues that interstitial brachytherapy using permanent seed is a promising treatment technique for lung cancer[16].

Brachytherapy offers a key advantage over external beam treatment modalities: the radiation dose is delivered directly to the diseased cells over the treatment period, without irradiating healthy tissues in front of the target volume. Although radiation

passing through the target volume still affects external (healthy) tissues, the dose rate (and hence total dose) decreases with the square of distance, in contrast to an external radiation beam which is nearly parallel (and which, for photon beams, deposits most of its dose near the surface).

Proper positioning of brachytherapy sources depends on three critical factors:

1. The choice of the radioactive source;
2. The required dose; and
3. The spatial distribution over which the dose is to be delivered [17].

2.1.1 High Dose Rate and Low Dose Rate Brachytherapy

If the treating physician decides that the patient is a suitable candidate for brachytherapy, two options are available: permanent implantation of many relatively low-activity and short half-life radioactive sources (known as *seeds* in this context), known as *low dose rate* brachytherapy (LDR BT); or temporary placement of a single high-activity source in various locations in the treatment volume, known as *high dose rate* brachytherapy (HDR BT). Both LDR and HDR brachytherapy techniques are widely used in treating different kinds of cancer; there is often no particularly compelling reason to choose one over the other, and the decision is often made on the basis of the personal preference and experience of the treating physician[13].

Insertion of the seeds (LDR) or source (HDR) is achieved via the pre-implantation of a series of thin plastic catheters or needles, positioned using an applicator. The seeds or source are then afterloaded into the treatment volume; for LDR BT the needles are then withdrawn leaving the seeds in place, while for HDR the source is first withdrawn and then the catheters are removed.

Due to the proximity of the radioactive sources to the target tissues, dose gradients in the target volume can be very high, due to the inverse square law. This enables the delivery of a highly conformal dose to the treatment volume with minimal dose to sensitive nearby tissues. Brachytherapy, therefore, can be performed on the scalp, prostate and other sites where conventional external radiotherapy techniques are sometimes less safe due to the proximity of highly radiation-sensitive tissues [14]. Brachytherapy sources and seeds come in many different shapes and sizes, and can be spherical, cylindrical or rectangular.

2.1.2 Low Dose Rate (LDR) Brachytherapy

In LDR brachytherapy, radioactive seeds are permanent implants, which emit radiation at dose rates equivalent to < 2 Gy/h [18]; depending on the half-life of the radioisotope, the seeds may continue to deliver a therapeutic dose to the treatment volume as its activity decays exponentially over a period of weeks to months [19]. LDR brachytherapy is most commonly performed using iodine-125 (^{125}I), palladium-103 (^{103}Pd), or caesium-131 (^{131}Cs) seeds encased in a non-radioactive metal casing (typically a non-reactive metal such as platinum or palladium).

LDR BT is suitable for treating many different types of cancer. Skowronek reports that LDR BT has been effectively used in treating localised prostate cancer for more then 30 years [4]. Kim et al. state that treatment of patients with carcinoma of the uterine cervix has been successfully performed using LDR-BT [19].

LDR BT treatment involves three main steps. Firstly, a treatment planning process, performed a few weeks before the planned implant date, is undertaken in order to calculate optimal positioning of the radioactive seeds. To do this, the precise shape and position of the tumour are measured, using one of a variety of different imaging and scanning techniques. For example, Bownes and Flynn report that prostate cancer volume can be imaged using a trans-rectal ultrasound (TRUS) probe [20]. The treatment planning system then computes the placement of radioactive seeds which will achieve optimal tumour ablation. Secondly, radioactive seeds with known activity are inserted into the target area through a needle placed into the correct position in the body via a template, carefully positioned relative to the tumour (verified using a CT or ultrasound scan). Once positioning is complete, a final CT scan is performed on the patient to determine the exact position of the seeds; if any significant under-dosing results from positing errors, a small number of additional seeds may be inserted.

2.1.3 High Dose Rate (HDR) Brachytherapy

In contrast to LDR BT, HDR brachytherapy uses a highly radioactive source, with a dose rate of of at least 12 Gy/h, which is moved around the treatment volume using a specialised robotic control unit attached to a series of pre-positioned catheters. An HDR BT treatment session typically takes between 1 and 30 minutes for a treatment using the most common HDR BT radioisotopes, iridium-192 (^{192}Ir) or cobalt-60 (^{60}Co) [4, 14].

The use of HDR BT has significantly increased worldwide over the past few years. Its effectiveness has been demonstrated for different types of cancer, including prostate, cervix, endometrium, breast, skin, bronchus, oesophagus, head and neck and many other kinds of cancer [21, 22]. HDR BT can be performed during several fractionated sessions and offers a lower level of late toxicity and rate of late complications compared to LDR BT. However, this fractionated schedule may result in more workload per patient [19, 21, 23]. In addition, sophisticated HDR afterloading equipment and expensive applicators are required to operate a HDR treatment facility. With current high-precision afterloaders, medical imaging systems and control software, the required dose can be delivered to the target volume with a high degree of accuracy, although there is still room for improvement [21].

2.1.3.1 Implantation Techniques

Many of the procedures for HDR BT treatment are quite similar to those used in LDR BT. Firstly, a pre-operative scan of the tumour region is performed to determine the volume and extent of diseased tissues. This can be performed using a range of imaging techniques, such as TRUS with appropriate treatment template planning software in the case of prostate implants [21]. A CT scan of the target volume is normally performed to confirm that the catheters penetrate the prostate at the correct locations, prior to commencing irradiation. Earlier HDR PBT protocols also often used fluoroscopes to confirm the location of the source; however these only provide limited information regarding the location of the source. Additionally, the use of CT for treatment planning in HDR brachytherapy. Based on the scan, source dwell times and positions are computed using treatment planning software (TPS), such that the desired tumour volume and margin will received the prescribed dose. Needles are used to insert catheters, typically aligned via a surgically-attached grid template, into the target volume (in the case of prostate cancer, the needles penetrate the perineum). A robotic afterloading unit is connected to the catheters, and feeds the source into the catheters one at at a time, stepping between the series of positions and dwell times determined by the TPS. One consequence of the short duration of irradiation at each source position is that it affords greater flexibility in dose distribution than is possible with LDR BT implants, which simply decay from the initial activity [20].

2.1.3.2 Isotope Selection

A variety of radioisotopes can be used as the source for HDR BT; however, ^{192}Ir and ^{60}Co are generally preferred in modern clinical practice. The energy range of the radiation emitted from these radioisotopes is well suited to radiotherapy applications in general and brachytherapy in particular, and both types of source can be fabricated with small dimensions suitable for brachytherapy applications [20, 22]. These isotopes are chiefly characterised by the energies and the types of radiation which they emit. ^{192}Ir and ^{60}Co both emit high-energy photons, with the former exhibiting a complex energy spectrum (mostly in the 300-500 keV range, with an average of 380 keV) and the latter producing photons at two main energies of 1.17 MeV and 1.33 MeV. The half-life of ^{192}Ir is about 74 days, compared with 5.27 years for ^{60}Co [22].

2.1.4 The Need for Real-Time QA in Brachytherapy

Fractionated HDR brachytherapy significantly relies on reproducible catheter positions for each fraction to ensure a maximum efficacy of tumour treatment while minimising damage to healthy tissues. A real-time source tracking system has the potential to significantly improve the consistency of HDR brachytherapy procedures, both by offering the potential for real-time correction of the delivery of a single fraction, or providing information to the TPS for the design of treatment plans for subsequent fractions, to compensate for any under-dosing or over-dosing in the previous fraction. A limited number of source tracking system currently exist which can provide some degree of real-time three dimensional source position information. Most of these methods are based on external (out-of-body) imaging systems, which either suffer from low spatial resolution, or require an acquisition time which exceeds the planned dwell time in some or all locations, limiting the usefulness of such devices for real-time source position [24–28].

While quality assurance is also important for LDR brachytherapy, it is less critical than for HDR brachytherapy since the seeds remain in position permanently. This means that the ability to correct the seed distribution after the implantation procedure is limited (although an extra seed may be added, it is impractical to remove those which have been already implanted); furthermore, if QA is required, it can be achieved via a post-operative CT or MRI scan (the seeds are non-magnetic and are generally MRI-safe). Therefore, **the remainder of this Thesis is solely concerned with QA systems for HDR brachytherapy.**

2.1.5 HDR Prostate Brachytherapy

By far the most common use of HDR brachytherapy is in the treatment of prostate cancer; it is also one of the most popular options for treatment of prostate cancer and having somewhat displaced LDR brachytherapy in this application due the greater flexibility of dose distribution which may be achieved through the use of variable dwell times. In addition, the use of HDR brachytherapy as a monotherapy is associated with decreased rate of acute urinary frequency, urgency, dysuria and rectal pain, while achieving tumour control equivalent to LDR [20, 21, 29, 30]. For this reason, the remainder of this thesis will use prostate brachytherapy as the reference treatment for evaluating the performance of the proposed source tracking system; however, its use is by no means limited to this application.

The human prostate has a normal volume of up to 30 mL, while an enlarged (pre-cancerous or cancerous) prostate may be up to double this volume [31].

2.2 Causes of Error in Source Positioning in HDR Prostate Brachytherapy

Positioning uncertainty in HDR PBT has been extensively investigated in the literature. Hoskin et al. identified three possible causes of catheter movement: external migration of the catheter through the skin, internal movement of the prostate and oedema build-up between the prostate apex and perineum [32]. The authors performed a study to determine the extent of catheter and prostate movement between two fractions over a period of 18 to 24 hours. A number of flexible plastic afterloading catheters with a length of 15 cm were implanted under the guidance of transrectal ultrasound. Catheters were placed at the skin in their planned positions using a flexible latex template with integrated O-rings developed by the authors. The latex template was adhered and sutured to the skin. All the patients underwent two CT dosimetric scans within 1-2 hours of the implant procedure prior to the delivery of each fraction. The authors reported the results for a total of 332 catheters implanted into 20 patients, with a median of 16 catheters used for each implant with a range of 14 to 20 [32]. The CT analysis shows that the mean inter-fraction movement of catheters relative to prostate is 11.5 mm (range 0-42 mm). This shows that there is a substantial change in prostate position between fractions resulting in a substantial under-dosage for the prostate in the second fraction. In order to avoid a significant reduction in the delivered second

dose fraction to the tumour, the authors recommended that the catheters should be placed roughly 1 cm beyond the base of the gland. They also highly recommended that a CT scan to be performed before each fraction of the treatment to allow adjustment to be made for cranial migration of the prostate gland.

Simnor et al. performed a study to evaluate changes in catheter position during HDR PBT treatment and to determine whether or not a repeated CT scan is needed before each fraction [34]. Between 14 and 20 flexible plastic afterloading catheters, each with a diameter of 2 mm, were implanted into 20 patients using the same flexible latex template which was developed by [32]. Patients were treated with 3 HDR fractions over 2 days, with the time interval between each fraction being 6 hours. A CT scan was employed before each fraction and a corrective action was performed for every patient by either shifting the dwell positions distally by the amount of catheter displacement or by physical re-advancement of the catheter. The authors used dose volume histogram (DVH) values of V100% and D90% for the planning target volume (PTV) and V100% for the clinical target volume (CTV), where V100% is the percentage of the prostate receiving of the prescription dose, and D90% is the dose delivered to at least 90% of the target volume. To asses the implant quality of fractions 2 and 3, data from 20 patients was analysed using SPSS (Statistical Package for the Social Science, version 16.0 for Windows, Chicago, USA) [34]. The findings show that the catheter movement relative to the prostate ranged from 0 to 21 mm with mean value of 7.9 mm and 0 to 25.5 mm with mean value of 3.8 mm for fractions 2 and 3, respectively. The results also show that the delivered dose to the tumour in fractions 2 and 3 significantly increased after the corrective action proposed by the authors. However, The authors discussed the limitations of the correction method, and indicated that it will enable effective dosimetry to be achieved only if the set of organs at risk (OARs) in subsequent fractions is the same.

Cury et al. assessed the change in the volume of the prostate gland after a single fraction HDR BT treatment [35]. The authors reported the variations in the prostate gland volume of 31 patients who underwent a single fraction HDR prostate brachytherapy. In 21 patients (68%), they found that the prostate volume increased by an average of 7.5% from a pre-treatment mean volume of 40.86±17.54 cm^3 to a mean post-treatment volume of 43.95±19.01 cm^3) after the single-fraction dose was applied [35].

In their study, Martinez et al. evaluated the volumetric changes that can occur in the prostate gland during the implantation and treatment procedure [36]. To calculate

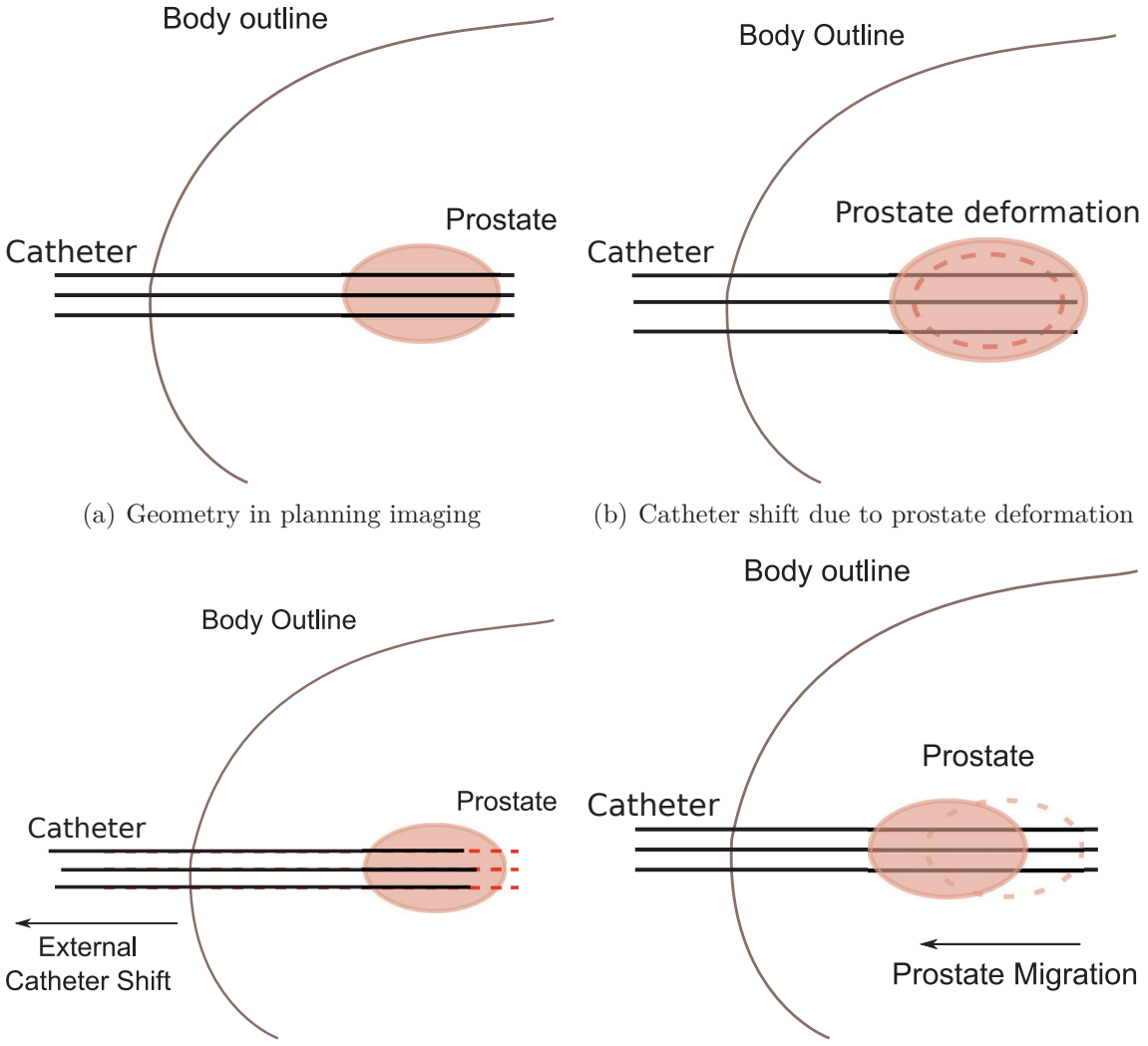

(a) Geometry in planning imaging

(b) Catheter shift due to prostate deformation

(c) Catheter shift external to patient's body

(d) Catheter shift due to prostate migration in the patient's body

Figure 2.1: Causes of catheter position shift relative to the prostate [33].

the changes to the volume of the prostate gland, the authors acquired three sets of axial TRUS images at three different times before the implantation procedure and during the treatment. The first set was obtained before any needles were inserted into the prostate, and the mean volume of the prostate gland was found to be 30.7 cm^3 (with the measured volume ranging from 21.5 to 41.6 cm^3). The second set was acquired after the placement of all needles and before any fraction was delivered, resulting in a mean value of the prostate gland volume of 38.2 cm^3 (with volumes ranging from 25.0 to 43.9 cm^3). The last set was captured at the end of fraction 4, yielding a mean prostate volume of 38.2 cm^3 (and a range of 25.7 to 47.8 cm^3). The authors used DVH to assess the implant quality; the mean D90% for fraction 1 and fraction 4 were 104% or 988 cGy (with a range from 95% to 120%) and 100% or 931 cGy (range from 86 to 112%), respectively. The authors conclude that changes in the interfraction prostate volume can be considered to be clinically insignificant. However, needle movement appears to have a significant effect on the delivered dose between fractions 1 and 2.

Dinkla et al. investigate changes in prostate volume during treatment by analysing catheter configurations on three successive scans [37]. A group of 31 intermediate and high risk prostate cancer patients was treated with EBRT (23 $\times$ 2 Gy), followed by a PDR (Pulsed Dose Rate) brachytherapy boost of 24.96 Gy. A number of catheters were implanted, depending on the volume of the prostate to be treated. Three CT scans were performed: the first CT scan was acquired 2 hours after implantation of all the catheters, while the second and the third CT scans were performed after 24 and 48 hours, respectively. To evaluate volume changes, the authors calculated the mean radial distance (MRD) of all dwell positions to the geometric centre of dwell positions. The results revealed that the relative volume change derived from the change in MRD was 4.3$\pm$6.4%, 4.4$\pm$7.5% and 0.6$\pm$3.7% between CT1-CT2, CT2-CT3 and CT1-CT3, respectively. This represents a mean volume difference of 1.5$\pm$2.8 cm^3. The authors claimed that the effects of the oedema on the dose delivered during the 48 hours of temporary prostate brachytherapy was limited.

2.3 The Physics of Source Tracking

A radioactive source, as used in brachytherapy, decays over time, releasing some combination of energetic particles (including helium nuclei or α particles, positrons or β^+ particles, and electrons or β^-) and photons (γ-rays). The energy of these particles and photons depends on the specific radionuclide undergoing decay; typically more

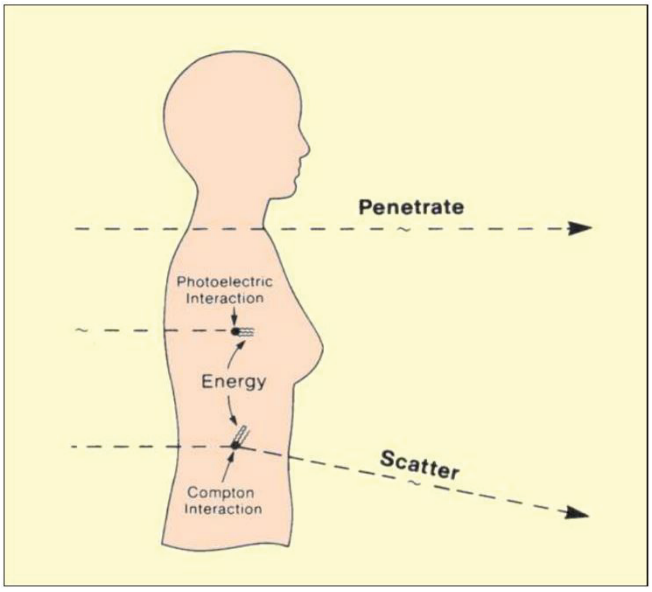

Figure 2.2: Photons interacting with the human body experiencing three possible modes of interaction [38].

than one energy of γ-ray is emitted, with each energy having a certain probability (branching fraction or ratio), resulting in a complex γ spectrum. The radioactive sources used in brachytherapy are sealed in a protective metal shell, which is sufficient to block all α and most $\beta^{\pm}$ particles. Therefore, the only significant dose is delivered via the remaining γ radiation.

High energy photons - either γ-rays, as produced by radioactive decay, or X-rays, as produced by rapid deceleration of energetic electrons directed at a metal target - interact with matter in several different modes; the probability of each specific mode for a given photon depending on its energy and the composition of the target material:

1. The incident photon can penetrate the object without interaction at all;
2. It can interact with matter and transfer all energy to an atom in the target; or
3. It can interact and be scattered or deflected from its original direction.

.

High-energy photons can deposit their energy in matter through two main types of interactions, both involving electrons. In the first, known as the *photoelectric effect*, the entirety of a photon's energy is absorbed by an atom in the target; in the second,

known as *Compton scattering*, some of the energy of the incident photon is transferred to an atom in the target, with the remaining energy re-radiated in a different direction as a lower-energy (longer wavelength) photon. Several other modes of interaction are possible, including Rayleigh scattering (elastic scattering, in which the direction of the incident photon changes but not the energy) and pair production (in which some of the photon's energy is converted into an electron-positron pair, which annihilate to produce 511 keV gamma photons). However, these are of limited interest at the photon energies normally produced by brachytherapy sources.

2.3.1 Photoelectric Effect

The *photoelectric effect* is an atomic absorption process in which an atom absorbs totally the energy of an incident photon[12]. This typically results in the ejection of an orbital electron from the atom. The ejected electron is called a *photo-electron*, and obtains kinetic energy E which is equivalent to the difference between the energy of the incident photon E_0 and the binding energy of the electron to shell from which it was ejected. In order for photoelectric absorption to occur, the incident photon energy must be greater than or equal to the binding energy of the electron that is ejected[39]. When an electron is ejected from an inner shell, the atom is ionised and a vacancy is created in this inner shell, which results in the transition of an electron from a shell with a lower binding energy. This transition creates another vacancy, which, in turn, is filled by an electron from an even lower binding shell. This difference in binding energy leads to the emission of characteristic x-rays. The sum of the characteristic x-ray energies equals the binding energy of the ejected photo-electron:

$$E_{pe} = E_0 - K_B \tag{2.1}$$

where K_B is the shell binding energy for the atom from which is ejected.

2.3.2 Compton Scattering

In *Compton scattering*, the incident photon interacts inelastically with an outer shell orbital electron of an atom. The incident photon is deflected through a scattering angle θ, transferring part of its energy to a *recoil electron* which is ejected from the atom [39]. Compton scattering leads to the ionisation of the atom and the division of the incident photon energy between the scattered photon and ejected electron. Consequently, the

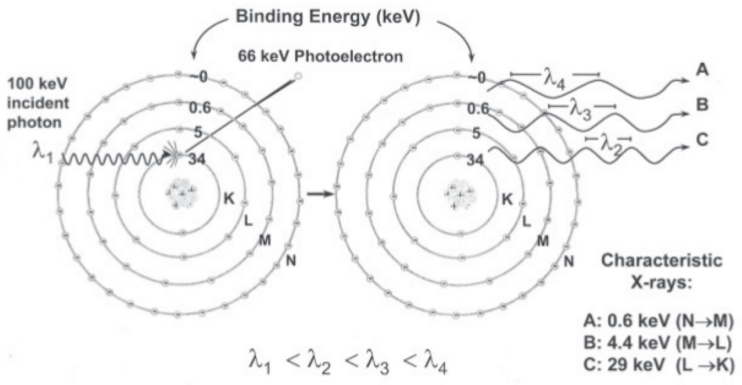

Figure 2.3: Photoelectric absorption. The diagram shows a 100-keV photon undergoing photoelectric absorption during interaction with an iodine atom [39].

ejected electron will lose its kinetic energy through the interaction with the atoms of the surrounding material while the scattered photon may traverse the medium without interaction, or undergo further interactions, either via photoelectric effect or other modes of scattering [12]. The energy of the scattered photon is related to the scattering angle θ and the energy of the incident photon according to the formula

$$E_{sc} = \frac{E_0}{1 + \frac{E_0}{0.511}(1 - \cos\theta)} \tag{2.2}$$

where E_0 and E_{sc} are the incident and the scattered photon energies in MeV, respectively, and θ is the angle of the scattered photon. The energy transferred to the recoil electron is:

$$E_{re} = E_0 - E_{sc} \tag{2.3}$$

When the energy and the direction of the incident photon are known, a mathematical expression describes the relation between the detected energy and the scattering angle. Since the photon may experience consecutive Compton scattering interactions in a detector, it loses energy until a photoelectric absorption terminates the process. Therefore, from the measured position and the energy consumed at each scattering point, the path of the photon on the detector can be tracked.

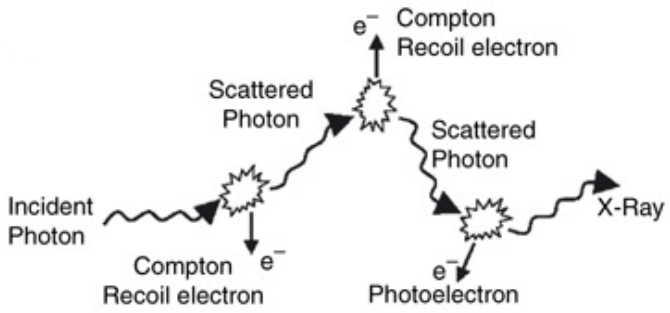

Figure 2.4: Multiple interactions of a photon passing through matter. Energy is transferred to electrons in a sequence of photon-energy reducing interactions [12].

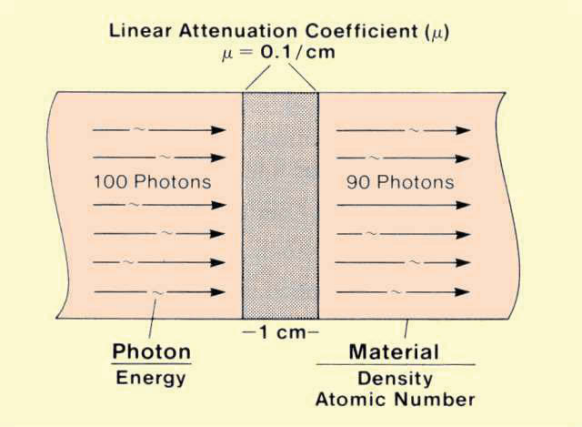

Figure 2.5: Linear Attenuation Coefficient [38]

.

2.3.3 Attenuation of Radiation

It is impossible to precisely predict how far any individual photon will travel before it interacts with matter, nor the type of interaction it will undergo. However, the probability of different types of interactions can be estimated, given the energy of the photon, the path length and the composition of the target. Therefore, for a given photon flux, the fraction of incident photons which will be absorbed and transmitted can be estimated.

Attenuation is the removal of a fraction of photons from a incident beam as it traverses a path through matter. Both absorption and scattering of the incident photons lead to attenuation. The fraction of incident photons removed from a mono-energetic incident beam of X-rays or gamma rays per unit thickness of absorbing medium is called the *linear attenuation coefficient* μ, which is expressed in unit of inverse distance (typically cm^{-1}). The value of the linear attenuation coefficient indicates the rate at which photons interact as they pass through an object, and it is inversely proportional to the average distance photons travel before interacting. The attenuation coefficient values can be determined by the energy of the individual incident photon and by the atomic number Z and density ρ of the matter.

The intensity I of a photon beam transmitted through a uniform medium of thickness x is:

$$I = I_0 e^{-\mu x} \tag{2.4}$$

where I_0 is the intensity of the incident beam and μ is the linear attenuation coefficient. μ is the sum of the attenuation coefficient due to Compton scattering, μ_C, and the attenuation coefficient due to the photoelectric effect μ_p:

$$\mu = \mu_p + \mu_C \tag{2.5}$$

Since it is often more convenient to express the attenuation in terms of the mass of the matter traversed by the photon beam rather than in terms of distance, the term *mass attenuation coefficient* (μ/ρ) indicates the fraction of photons which will be absorbed, in units of area per unit mass (typically cm^2/g) of the material.

$$\text{Mass Attenuation Coefficient} = \frac{\text{Linear attenuation Coefficient}(\mu)}{\text{Density}(\rho)} \tag{2.6}$$

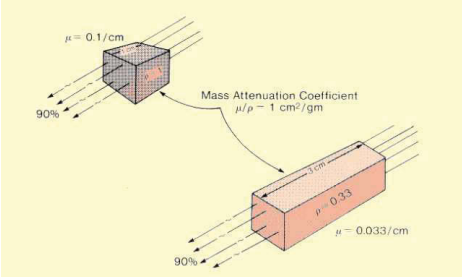

Figure 2.6: Mass attenuation coefficient [38]

2.4 A Survey of Nuclear Medical Imaging Systems

This section discusses several imaging techniques which can be used both for treatment planning and also for measuring the position of catheters or a brachytherapy source, both for HDR and LDR brachytherapy.

2.4.1 Computed Tomography (CT)

Computed tomography (CT) is a widely used and extremely valuable diagnostic tool for many clinical applications. In CT, an external X-ray source emits a fan-shaped beam of radiation through a target. The intensity of the incident X-ray beam and transmitted X-ray beam is measured at different angles using a photodetector array on the opposite side of the target - this is cumulatively known as a view or *projection*[40]. Each point in the projected image space represents the total X-ray attenuation properties of the target as measured along a line between the X-ray source and the point on the detector array. Multiple projections through the target are obtained at different angles; the three-dimensional structure of the target is then reconstructed using an algorithm such as filtered back-projection (an inverse Radon transform with ramp filtering) or one of a number of high-performance iterative algorithms which seek to minimise imaging artefacts[11]. CT imaging provides excellent spatial resolution and is well-suited to imaging bone or other tissues where there is a large difference in X-ray absorptivity.

Several authors have evaluated the application of CT-based treatment planning for HDR and LDR brachytherapy. Schnapauff et al. designed a study to evaluate clinical outcomes for patients with irresectable, intrahepatic cholangiocarcinoma (IHC) treated with CT-guided HDR brachytherapy for local tumour ablation [41]. The key finding was that CT data-sets can be used to prepare precise 3D treatment plans to cover the whole tumour volume, while limiting radiation exposure to healthy tissues; CT-HDRBT

was also shown to be appropriate for treating large tumour volumes. Zhongmin et al. examined the efficacy of CT-guided LDR prostate brachytherapy seed implantation therapy in patients with unresectable tumours, finding that highly effective and safe radiation doses can be applied to the tumour cells by implanting ^{125}I seeds under CT guidance [42]. Similarly,

While CT provides excellent spatial resolution, in particular for objects with high X-ray absorption contrast against human tissue, it necessarily delivers a significant radiation dose to the entire volume of interest. While this exposure may be considered an acceptable risk associated with the preparation of a high quality treatment plan, it is always desirable to minimise patient radiation exposure as much as reasonably possible. Therefore, the use of CT for *real time* quality assurance in HDR (or LDR) brachytherapy is not feasible in practice. It may be appropriate for post-operative verification of LDR seed positions (and due to the high contrast between the seeds and surrounding tissue, a lower X-ray dose could potentially be used for this application compared to a general diagnostic imaging dose).

2.4.2 Ultrasound

Due to its inherent safety and relatively low costs, ultrasound imaging is a standard tool for pre-operative treatment planning and intra-operative guidance and position verification during brachytherapy procedures [43, 44]. . A TRUS probe can be used during US guided procedures, both for treatment planning and for real-time guidance of needle insertion. The TRUS probe is a suitable imaging device to investigate the influence of possible anatomical variations which may occur between the planning process and the treatment delivery [43]. [43].

Carrara et al. investigated whether intra-fraction changes in the geometry of the catheter (needle) between initial imaging and delivery of the therapeutic dose are correlated to discrepancies between measured and planned dose during TRUS-guided HDR-BT treatment [43]. Implantation of OncoSmart Proguide catheters (2 mm in diameter) was performed according to a virtual plan developed using on preliminary TRUS images of the prostate. A total monotherapy dose of 28 Gy was delivered to a number of low to intermediate patients through two fractions of 14 Gy each. The relative difference between the planned and measured dose ranged from -19.5% to 15.8%; moderate correlation between this difference and the catheter displacement was found (of 0.64 (or 0.74 if measurements were weighted for dwell time and proximity to the dosimeters). In general, the shift in catheter position between initial imaging and

treatment delivery was in the direction of the rectum, resulting in increased doses to the radiosensitive rectal wall compared to the treatment plan. This strongly supports the need for real-time QA during an HDR brachytherapy procedure.

Schmid et al. evaluated the accuracy of the needle implant position reconstructions based on TRUS images [45]. 10 to 18 plastic needles, each 2 mm in diameter, were implanted into six phantoms under the guidance of TRUS images. Both 3D TRUS images and CT scan images of the implanted phantoms were obtained. The differences between the reconstructed dwell positions in the US data set and the corresponding locations in the CT data set were compared and the results were evaluated based on a number of dosimetric parameters, including D_{90}, the dose, which covers 90% of the prostate volume, V_{100} and V_{150} (percentage of the prostate volume enclosed by 100% and 150% isodose). The median difference between the dosimetry estimates obtained from both image modalities is relatively small (0.5 mm), with the majority of differences less than 2.0 mm. The authors discuss the limitations of their technique and indicate that the major discrepancy when applying the Vitesse software is a systematic error in defining the radial position of the needle. This causes the needle channel to be reconstructed at a distance of 1 mm closer to the probe than as determined from CT imaging. This systematic error was then corrected by making a straightforward static correction in the radial direction to compensate. This results in a significant reduction in the discrepancies between the two data sets, from 10% to 2.2%.

2.4.3 Dosimeters and Source Tracking Methods in HDR Brachytherapy Treatment

Several dosimetric and imaging systems have been proposed to provide an estimate of the delivered dose distribution or to verify the source position. Although thermoluminescent dosimeters (TLDs) have been used extensively to verify the absorbed dose at a given location of interest, these passive dosimetry systems are incapable of providing measurements in real time [46–48]. A second approach is to use an external solid-state semiconductor radiation detector system to monitor the source position for quality assurance (QA) in HDR PBT. Since the dose rate from an isotropic radiation source is inversely proportional to the square of the distance to the detector, this may result in either a significant uncertainty in the estimation of the source location or an acquisition time exceeding that needed for real time source tracking [48, 49].

An alternative approach is to insert a compact radiation sensing system into the patient in close proximity to the treatment volume. Several methods have been proposed for in-body real-time HDR brachytherapy QA using different kinds of detector or dosimetry systems, such as MOSFETs, diodes and plastic scintillation detectors. These systems have been shown to perform well; however, uncertainty in the detector position may result in a significant error in the determination of the source location [50]. Lambert et al. reported that although diamond detectors offer adequate sensitivity for HDR-PT QA and good radiation resistance, they are impractically bulky, rendering them unsuitable for in-body applications [48]. The diamond detector also exhibited significant dose rate dependence and non-linearity at higher dose rates [51].

To identify a source location in three-dimensional space inside a patient, Nakano et al. proposed a new approach using a diamond detector and an array of three calibrated dosimeters [52]. In this work, they placed a diamond detector 1 cm from an encapsulated ^{192}Ir source with dimensions of 0.6 mm $\times$ 3.5 mm, and a calculated pre-irradiation dose of approximately 15 Gy. The relatively small size of their diamond detector results in high spatial resolution, and its high sensitivity makes it suitable for providing real-time source localisation data. For source position identification, three detectors were placed perpendicular to the catheter axis. While the radioactive source inserted in the catheter remained stationary, the diamond detectors were moved along a line perpendicular to the catheter axis. The obtained readings were then expressed as a function of the distance between the catheter and the source, and compared to the expected detector readings. The findings indicate that for a better source position verification, the distance between the diamond detector and any point on the catheter must be in the range of 1-12 cm.

Real-time dosimetry systems based on diode detectors have previously been used in HDR brachytherapy treatment. Although these systems offer rapid processing time and robust accuracy, their sensitivity is highly dependent on distance to the source [6, 51, 53]. Seymour et al. investigated the use of a dosimeter consisting of an array of five PTW diodes for estimating the the dose delivered by a HDR-PBT source inside the rectum [54]. Dose values for 28 patients were measured, and the deviations between the device measurement and planned dose in 71% of the measured points were $\pm$10%. However, the error increased to $\pm$20% when the number of the measured points increased from 71.1% to 95%. The results show that this system is only suitable for selected patients as it is not always capable of being applied in subsequent fractions; it is also only able to provide measurements about gross error in the delivered dose

rather than determining the distribution of that error. A further shortcoming of this approach is that the high degree of directional dependence of the diodes as the source to the diode array angle increases can significantly degrade the accuracy of the results.

Multi-point MOSFET detectors have been investigated for real-time dose measurements during HDR PBT. The small physical size and good spatial resolution of these detectors, in addition to their ability to provide immediate readout, make them a promising candidate for QA in HDR-PBT [6, 48, 53, 55]. However, the variation in sensitivity of the recorded dose, the non-water equivalence of the detector and the angular dependence of MOSFET detectors limit the use of this system for accurate in-body brachytherapy dosimetry [48, 51, 56]. A study using micro-MOSFETs for in-body dosimetry was performed by Qi et al. to evaluate the dose received by a patient undergoing HDR intracavitary brachytherapy of nasopharyngeal carcinoma (NPC) [53]. They investigated the use of an array of five MOSFETs which were calibrated independently in a water phantom, resulting in dose calibration factors of 0.46±0.012 Gy/mV for the ^{192}Ir source. Dose values for 11 NPC patients were obtained with a good agreement with the predicted dose measurements of -0.3± 3.9% (right side) and -0.3±3.7% (left side).

A clinical *in-vivo* dosimetry system has been assessed and error detection thresholds for real-time HDR brachytherapy treatment monitoring have been investigated by Mason et al. using intra-operative trans-rectal ultrasound (TRUS) with a microMOSFET placed into an additional needle [57]. To assess the errors between the planned and delivered doses which are caused by the movement of the needle, they have performed an uncertainty analysis including Monte-Carlo simulations. The results have shown that an error of 1 mm occurs between the predicted and the measured doses because of the movement of the needle, and this shift does not have a significant impact on the planned treatment. However, some errors could not be detected, making it difficult to evaluate the impacts on total dosimetric error.

A recent dosimetric study involving the use of MOSkin detectors was conducted by Gambarni et al. to perform real time *in-vivo* dose measurements during the brachytherapy of the prostate [6]. They conducted their experiments inside a urethral catheter in a gel phantom (emulating a real prostate) and using an ^{192}Ir radioactive source with active length of 3.6 mm. Single and dual-MOSkin detectors were calibrated in a water phantom at a distance of 38 mm from the source. The maximum discrepancy between planned and measured dose was 8.9% and 3.8% for single and dual MOSkin detectors respectively.

Plastic scintillation detectors (PSDs) have been proposed as a mechanism for real-time verification of HDR brachytherapy treatment. Since plastic scintillation detectors are compact and water-equivalent, while providing good dose linearity, independence to dose rate, fast response, temperature independence and energy independence above 100 keV, plastic scintillation detectors are an attractive candidate for in-body dosimetry and imaging [56, 58, 59]. A clinical study conducted with an in-body plastic scintillator detector system was performed by Therriault et al. to determine the feasibility of using PSDs for QA during ^{192}Ir HDR prostate brachytherapy treatment [51]. The proposed system consists of a green plastic scintillator fibre, 1 mm in diameter and 3 mm long, coupled to a light-shielded 1 mm×7 mm optical fibre. A total of 13 parallel catheters were inserted in a 35 cm×35 cm×25 cm water phantom, and the ratio of the measured dose in 43 specific dwell positions with dwell time of 5 s compared to the dose predicted by the treatment planing system (TPS). The dosimetry system recorded a delivered dose of 99.6±3.2% to 100.5±1.5% and 104.3±0.3% of the planned dose in the urethra and the rectal wall, respectively.

A second design based on PSDs, known as *Brachy*FOD, was described by Cartwright et al., in which an insertable applicator was developed for in-body use which provides real-time dose mapping and source tracking of an HDR prostate brachytherapy source [58]. In this study, the deviations between the planned and the absorbed dose were found to range from 2% to 3%, and the average error between the predicted and the calculated source position was approximately 2 mm. However the authors noted that the error in estimating the source position can be up to 9 mm when the distance between the source and the scintillator is more than 100 mm.

Duan et al. investigated the use of a pinhole-based imaging system for in-body monitoring and verification of ^{192}Ir HDR brachytherapy [60]. The developed system consists of a pinhole collimator combined with an X-ray fluoroscope and a radiographic film-screen. This system can recognise source images for dwell times ranging from 2 to 400 s, with an error between the planned and reconstructed dwell positions varying from 0.3 to 0.79 mm. However, the authors discussed the limitations of their technique and indicated that their method is not applicable in clinical cases of short dwell times due to the limited dynamic range of the screen-film combinations. It is also not able to provide real-time source tracking capabilities as the film image cannot be accessed until after the procedure is completed.

A similar source tracking system capable of real-time measurement was built by Batic et al. using two pinholes and two silicon detectors to localise a high dose rate

^{192}Ir source during BT treatment [61]. This method was able to reconstruct absolute coordinates of source positions in a volume of 20 cm × 20 cm × 20 cm^3 with a precision of about 10 mm. This alternative system solved the projection overlapping issue observed in Duan's method.

Lee et al. developed a tomo-synthesis-based seed localisation method using shape control function-based modified distance map images. This method can recover all sources locations automatically. However, it requires a large number of images compared to a the 2-D image-based approach [62].

Song et al. developed a prototype device which comprises a single flat panel detector and a tray of BB pellets to derive the 3D position of a radioactive source by analysing the shadow of the BBs on the flat panel [63]. Conceptually, this is similar to the idea proposed in this Thesis; however, the detector array is outside of the body, and the source localisation algorithm is rather limited, being based on shadow centres-of-mass only (and therefore ignoring valuable information contained in the image).

More recently, Wang et al. proposed an HDR source tracking method based for experimental evaluation of a proposed treatment plan using an instrumented phantom the fitted with two GaN dosimetric probes. The probes are used to measure the dose rate, through which the source position may be estimated [64]. For this system, a cumulative average of counts as recorded by the GaN SiPM during each dwell time, followed by a linear transformation were used to measure the dose rate. The obtained data was compared to the planned dose rate and used to estimate the source location. The detector configuration has also been proposed for in vivo real-time dose verification, although this has not been implemented yet.

In their study, Leeuw et al. have developed a MR imaging method, dubbed centre-out radial sampling with off-resonance (co-RASOR) [65]. In this method, the brachytherapy source can be tracked in 3D with millimetre accuracy with minimum dwell times of approximately 4 s. The method is a derivative of that originally proposed by Seevinck et al. in 2011, in which MR imaging was used to track the sources [66]. However, several minutes were required to acquire each image, rendering it unsuitable for real-time source tracking. In order to reduce the acquisition time, the authors applied two orthogonal 2D centre-out encoded slabs containing an ^{192}Ir source instead of the 3D centre-out design as proposed in the previous approach. This allowed localisation accuracy to be maintained while greatly decreasing the acquisition time. A CT scan was applied and compared to the results obtained from the developed MR imaging technique, showing

that the proposed method can achieve sub-millimetre source tracking accuracy in approximately 4 s.

Radiochromic films offer a number of advantages over other dosimetry techniques for both HDR and LDR brachytherapy treatment, such as high spatial resolution and low energy dependence [67–69]. Palmer et al. evaluated the use of Gafchromic EBT3 film as a dosimeter to perform quality control verification (QC) of a HDR treatment planning system and delivery equipment [70]. Gafchromic EBT3 was employed for all measurements of the HDR treatment unit; the source was ^{60}Co and could deliver a maximum dose of 50.8 Gy to the target volume. Ten films were exposed to a dose ranging from 0 to 5.8 Gy. To eliminate non-clinically relevant dose levels from the analysis, a lower dose limit threshold of 50 cGy was set for the gamma dose calculations. The author proposed a two-object test design: a three-channel block comprising two 150 × 300 mm^2 slabs of solid water with respective thicknesses of 20 mm and 5 mm, and a film array water phantom. HDR catheters with external diameters of 3 mm were accommodated into the phantom. The two test objects were placed in the centre of a 60 cm × 50 cm × 40 cm water tank while the measurements were being recorded. A dose of 1 Gy at 20 mm from the source axis was measured and the dose map generated using FilmQApro software according to the proposed method by [71]. Uncertainty analysis was performed based on the distance between the source and the film position. The standard uncertainty was found to be 3.5 % and 6.6 % at a distance from the source of 15 mm and 5 mm from the source, respectively. The authors compared the dose measurement results to published Monte Carlo data [72], finding that they are in good agreement. However, the results showed that when films are exposed to doses below 40 cGy, noise and deviations from TPS data increased. The authors also discussed that the proposed system is sensitive to simulated errors in the delivered dose, resulting in significant reductions of gamma passing rate.

Chiu-Tsao et al. investigated the use of radiochromic film in determining 2D dose distributions for ^{125}I seeds in LDR brachytherapy [69]. The authors used four ^{125}I seeds with an outer diameter of 0.84 mm and an active length of 3.76 mm. Each seed was placed in the centre of a 30 × 30 × 20 cm^3 solid water phantom. The centres of the active emulsion layer of each radiochromic film sheet were assumed to be the effective measurement points. The films were grouped into three categories: calibration films, experimental films and background film. A series of 25 film exposure experiments were performed using one of the four ^{125}I seeds, with an exposure time ranging from 4 hours to 593 hours. A comparison between two sets of calibration

films was conducted. While the first set was exposed to one ^{125}I seed at a fixed geometry, the other set was irradiated by a 6 MV photon beam. The authors employed a CCD-camera-based microdensitometer with interchangeable green and red lights with wavelength of 520 nm and 665 nm, respectively, to scan all the films. The obtained measurements were analysed, and dose conversion from net optical density (NOD) was performed according to the established ^{125}I calibration curve and the corresponding function fit for each experimental film. The calibration curves, which quantify the relationship between NOD and dose (in Gy) for both ^{125}I and the 6 MV photon beam, were obtained and visualised. It was found that the curves for these two energies were similar for the same light source. An uncertainty analysis of the experimental procedure was performed, it was found that the uncertainty of the dose rate constant was 6.9 % and 6.8% for green and red light, respectively. This study demonstrated the feasibility of using EBT film in measuring 2D dose distributions around ^{125}I seeds in a solid water phantom within a reasonable timeframe. However, the authors noted that EBT film was not able to measure the dose contribution from the 4.5 keV X-rays.

2.5 HDR BrachyView

The most promising innovation for HDR PBT QA is the BrachyView family of devices, developed at the University of Wollongong's Centre for Medical Radiation Physics, with two separate variants proposed for HDR and LDR PBT by Safavi-Naeini et al. and Petasecca et al., respectively [26, 73]. HDR BrachyView performs real-time monitoring of the position of the ^{192}Ir source during HDR prostate brachytherapy treatment.

The probe consists of a semi-cylindrical tungsten collimator with a linear array of symmetric biconical pinholes, suspended 6.5 mm over a 4×1 array of *Timepix* pixellated silicon detectors (256×256×4 pixels, 60×15 mm, with pixel pitch of 55μm). Source tracking is performed by locating the centres of mass of each projection of the source on the imaging plane, back-projecting lines through the pinholes, and identifying the point of maximum convergence. The probe's performance has been demonstrated both via Monte Carlo simulation and experiments with phantoms, with the maximum overall error between the planned and measured source position being 1 mm for the majority of evaluated source positions located in the target volume (a 40 mm×40 mm×40 mm volume above the detector). However, the error in estimated source position increases when the distance between the detector and the source is larger, reaching 1.3 mm for a source which lies in the extreme corners of the treatment volume. Sensitivity also varies

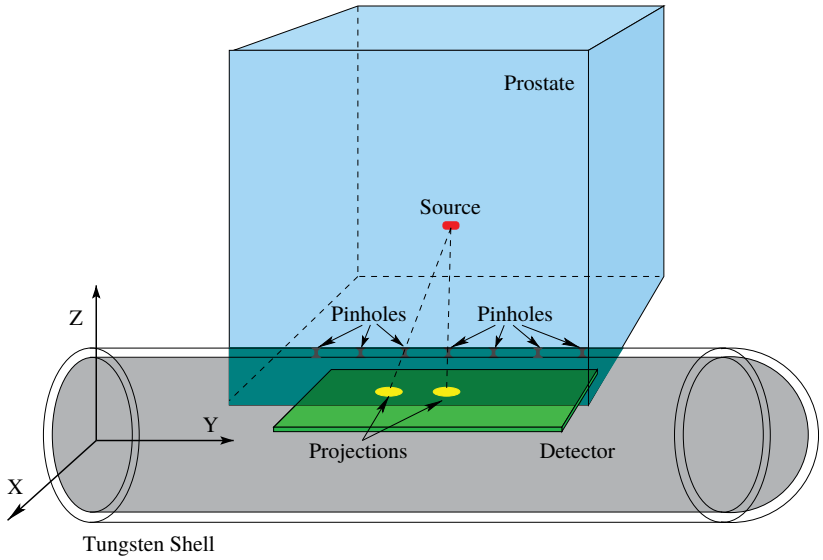

Figure 2.7: Schematic diagram showing the HDR BrachyView probe relative to prostate phantom [27].

depending on the arrival angle of the photons at the pinholes, restricting its field of view (FoV) to the acceptance angle of the double-cone pinholes; therefore, to monitor the entire potential treatment volume, it may be necessary to mechanically rotate the probe in situ, depending on whether the source will move beyond the detector FoV for a single angular orientation of the probe. Finally, due to the fact that most incident photons are blocked by the collimator, overall detector sensitivity is limited by the size of the pinholes (as there is an intrinsic trade-off between sensitivity and pinhole camera resolution [74]. The minimum acquisition time needed to obtain images of sufficient quality for sub-millimetre tracking accuracy is around 300 ms.

In the remainder of this section, the components and characteristics of HDR BrachyView will be discussed, with a particular focus on those of greatest relevance to the work described in this Thesis.

2.5.1 Pixellated Silicon Detector

A compact and scalable pixellated silicon detector system with integrated high-speed readout electronics and a high spatial resolution is required in order to provide high quality real-time imaging of the spatial distribution of radiation. The dwell time of the radioactive source in HDR brachytherapy treatment is typically of the order of seconds, and source activity is of the order of hundreds of GBq; therefore, real-time QA for HDR brachytherapy requires fast acquisition and transfer of image data in order to

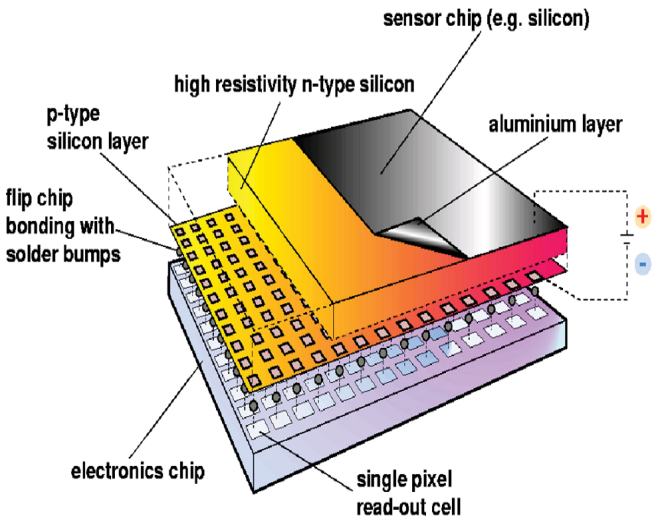

Figure 2.8: The Timepix ASIC chip. The sensor chip is bump-bonded to the readout chip. Wire bonds are visible[75]

avoid problems with saturation of the detector's counters. Furthermore, a detector system with a high spatial resolution is also essential to achieve accurate imaging of the radiation distribution, particularly when the source is further away from the detector.

The *Timepix* detector is an integrated radiation sensor resulting from the well-known Medipix2 detector, a commercial spin-off based on detectors developed at CERN for high-energy particle physics experiments [26, 76]. Timepix consists of a pixellated sensor chip (which may be silicon or cadmium telluride), bump-bonded to a readout chip which converts ionising radiation into current pulses which can then be characterised in terms of time of arrival or time over threshold (corresponding to energy) and read out via a USB or Ethernet interface. The pixels on Timepix detectors have identical dimensions to those of Medipix2 - however, the pixels offer an extended range of functions compared to the original Medipix2 design. Each Timepix detector consists of a 256×256 array of square pixels, each measuring of 55μm×55 μm^2. Each pixel cell contains approximately 550 transistors and the static power consumption is about 13.5 μW [26, 76–79].

One of three different types of information can be obtained from measurements in an individual pixel. Firstly, each pixel could provide information about the count of detected particles. Secondly, it can operate in Time over Threshold (TOT) mode, which provides information about the energy of particles detected in each pixel (that is, spectroscopic information). In the final mode of operation, it can provide information

about the arrival time of the detected particles in each pixel (Time of Arrival, ToA mode) [75].

Each Timepix pixel has its own integrated low-noise pre-amplifier, which enables high sensitivity to low energy X-ray photons. It also features a discriminator which can be used to eliminate noise and select only the energy which is of interest, resulting in low-noise single photon detection with pre-selected photon energies. A digital counter associated with each pixel can be used to count the number of detected photons, measure the particle energy or record the time of detection [26, 77, 79]. Importantly, Timepix can perform readout via a high-speed USB2 interface at frame rates of up to 100 full frames per second; at the completion of each frame read-out, the counters are reset. Multiple frames may then be combined in software on the host computer.

Due to its ability to perform per-pixel spectroscopy, the Timepix detector is able to distinguish between different materials of the same electron density such as PMMA and water, when back-illuminated via a calibrated broad-spectrum X-ray source [78, 80]. K.J. Loo et al quantitatively evaluated the application of *Timepix* detector as a soft tissue imaging and recognition system [76].

Timepix detectors are available singly or in gap-free arrays (currently with a maximum array size of 10×10 detectors). In particular, a 4×1 linear array is available which is suitable for use in a rectal probe such as HDR BrachyView or the related design proposed in this Thesis.

2.5.2 Collimator

The second main component in HDR BrachyView is the *multi-pinhole tungsten collimator*. This collimator is a cylindrical tungsten shell, 4 mm thick and with an external diameter of 24 mm, and separated into two halves along the axis of rotation to allow for milling of the pinholes and for insertion and removal of the detector array. Seven equidistant double-cone pinholes are drilled into the cylinder, in a line parallel with the axis of rotation with a centre to centre spacing of 6.5 mm. A PCB on which four gap-free Timepix detectors are tiled is mounted inside the collimator, with the detector plane passing through the axis of rotation, but with the detectors slightly offset laterally in order to accommodate the wire bonds from the Timepix chips to the PCB. Unfortunately, this necessitates drilling the double-cone pinholes off-centre as well, such that they are directly above the centre of the detector.

Pinhole geometry has been chosen on the basis of a trade-off between acceptance angle, sensitivity and spatial resolution [74]. The performance of a pinhole collimator

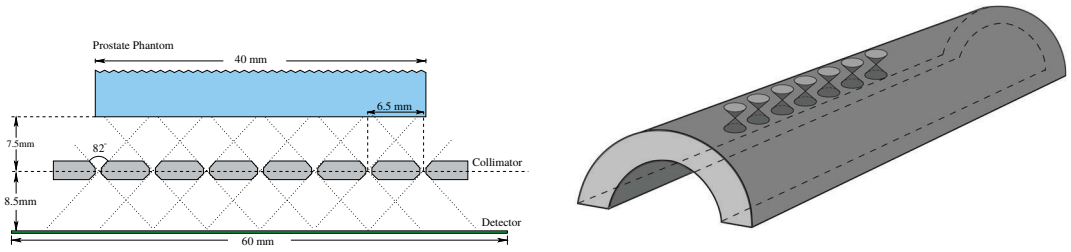

(a) Pinhole array schematic (b) Collimator design

Figure 2.9: Multi-pinhole collimator hole spacing[26]

.

involves trade-offs between each of these parameters. The field of view is chiefly limited by the acceptance angle; however, too large an acceptance angle will result in degraded image resolution as more photons will be able to directly penetrate the larger thin wedge of material near the centre of the pinhole. Increasing the degree of overlap between the cones (or the size of the cylindrical channel between them) also can increase the sensitivity at the cost of spatial resolution.

2.5.3 HDR BrachyView Source Localisation Algorithm

When γ rays traverse the collimator, an inverted image of the source distribution is projected onto the detector (with some background glow due to the imperfect attenuation of the tungsten collimator) [26]. The coordinates of the centre of mass of each visible projection are estimated by segmenting the image, and lines are back-projected from these locations through the corresponding pinholes to find the point of maximum convergence in the space above the detector plane. This is the best estimate of the source location. Since not all projections are necessarily visible on the surface of the detector (either because the source may be outside of the acceptance angle of some pinholes, or because the projection does not lie within the area of the detector), the correct pinholes through which a given image has been projected may not be immediately obvious; however, the order of the projections and pinholes is always the same. Therefore, a the same optimisation process is performed on a limited number of projection/pinhole combinations, and the solution which is the closest to the brightest projection is chosen as the correct solution.

2.5.4 Limitations

HDR BrachyView is currently the best option for in-body source tracking for HDR prostate brachytherapy. The basic concept has been shown to be sound, both theoretically, in simulation, and via experimental studies in phantoms. Nevertheless, there are a number of ways in which the design may be improved, either to improve performance, to simplify manufacturing or to simplify operation.

1. It is known that there is a small but systemic error in determining the source location; there is an error in the position estimation which is due to the intrinsic properties of the chosen source localisation algorithm rather than noise or other random effects. The chief cause of this is that at oblique angles, projections through a double-cone pinhole are significantly distorted. The optical centre of mass of these projections is not necessarily the same as the geometric location of the intersection between the detector plane and a line passing through the centre of the source and the centre of the pinhole. As the projections become more oblique, this deviation increases. Furthermore, when the source is in close proximity to the collimator, the increased number of directly-penetrating photons (i.e. those which pass through the body of the tungsten collimator) introduce a non-uniform brightening directly under the source (where the path through the collimator is shortest). These photons cannot be separated easily from the projected images, and introduce a further displacement to the optical centre of mass. **Development of a simpler, more direct source localisation algorithm offers the potential of avoiding this systemic error and providing a more consistent estimate of the source location.**

2. The tungsten collimator itself blocks approximately, (86.5±0.5)% of the incident photons [26], resulting in low detector sensitivity. Acquisition of a sufficient number of photons to achieve sub-millimetre accuracy in source localisation requires at least 300 ms of acquisition time (or more for a higher-quality image). **Reducing image acquisition time** may increase the range of treatment plans to which real-time QA can be applied, or alternatively *obtaining a higher quality image for a given acquisition time* should improve the accuracy with which the source can be tracked.

3. System sensitivity is non-linearly dependent on the angle at which an incident photon passes through the pinhole, as the amount of tungsten through which the

photon must pass to reach the imaging plane varies non-linearly as the source moves in space above the probe. The net effect is to degrade the accuracy of source tracking as the source moves away from the central axis of the probe. Therefore, **reducing the dependence of detector sensitivity on the photon's angle of incidence** should improve the uniformity of accuracy in position estimation.

4. The angle of arrival is limited by the geometry and position of the pinholes; furthermore, as a negative space, the pinholes also cannot be easily relocated on the collimator to suit a particular tumour location in a specific patient. To cover a wide field of view, it may be necessary to rotate the probe in situ and perform multiple >300 ms acquisitions. **Increasing the field of view should significantly help to speed up image acquisition and will simplify the mechanics of operating the probe.**

In addition, there are also significant practical problems; accurately machining seven perfectly-aligned double-conical pinholes in a tungsten cylinder is extremely challenging, not only due to the hardness of tungsten (necessitating the use of diamond drill bits, laser ablation or electron beam machining), but also due to the need to drill the holes off-centre to accommodate the detector PCB. Due to these problems, mechanical machining will not result in perfectly aligned pinholes, necessitating a calibration procedure in a uniform radiation field (which can be performed using a linac). As the devices are not expected to be manufactured in high volume, machining a small number of tungsten collimators with high precision is both expensive and time-consuming. For this reason, **changing the collimation system to one which can utilise simpler generic components and potentially exploit the rapidly developing field of additive manufacturing** will reduce manufacturing costs and increase manufacturing uniformity and repeatability.

2.6 Conclusion

In this chapter, the treatment of cancer (and prostate cancer in particular) using high dose rate brachytherapy has been discussed. The importance of reliable and accurate real-time 3D quality assurance (QA) system for monitoring the source location during HDR-BT treatment was discussed, including a review of the the leading methods used for source tracking. The design of HDR BrachyView, which is the leading

device currently available for this purpose, was described, and a number of potential opportunities for improvement were discussed.

In the following Chapter, the design of a proposed derivative of HDR BrachyView, *BrachyShade*, will be discussed in detail.

CHAPTER 3

Methodology

The probe described in this Thesis is primarily intended for use in prostate brachytherapy, as per the original HDR BrachyView probe. In principle, the same approach to source tracking could be adapted to HDR brachytherapy treatment of other organs, such as the cervix or oesophagus, where a probe could be positioned close to the treatment volume via a nearby body cavity. However, to provide a useful benchmark for comparison with published capabilities and accuracy of HDR BrachyView, the probe design and simulation model described in this Chapter are specifically configured for HDR prostate brachytherapy.

Section 3.1 describes the physical design of the probe. Section 3.2 introduces the error-minimisation algorithm used to estimate the source position based on the observed photon map acquired by the detector. Section 3.3 describes the analytic model which is used by the proposed error minimisation algorithm, while Section 3.4 discusses the Compton scatter correction algorithm which has been developed to improve the accuracy of the error-minimisation algorithm. Section 3.5 introduces a second alternative algorithm for position estimation, based on a hierarchical pattern-matching algorithm; some limited test results for this method are also presented in Chapter 4. Section 3.6 describes the simulation which has been used to both provide data for the Compton scatter correction algorithm, the results of which are presented in Chapter 4. Finally, Section 3.7 summarises the Chapter.

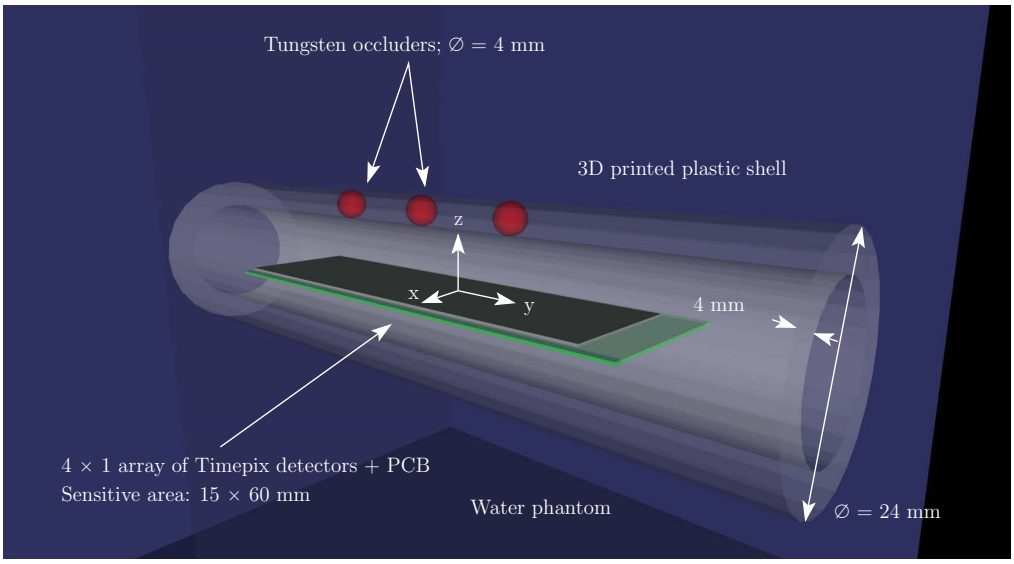

Figure 3.1: The BrachyShade probe with 3 occluders.

.

3.1 Probe Design

While HDR BrachyView uses a pinhole camera design, BrachyShade takes the opposite approach. A series of tungsten occluders, embedded in a low-density polymer shell above the detector plane, cast shadows on the detector. Images acquired from the detector are then analysed, and the observed photon distribution is then used to estimate the source location using a variety of methods which are discussed in this Chapter.

The detector consists of a linear 4×1 tiled array of edge-to-edge silicon Timepix modules, with wire bonds connecting them to the supporting printed circuit board on which the chips are mounted; the PCB includes a USB 2.0 interface for fast data transfer to a host computer. The detector array is positioned in the centre of a cylindrical plastic shell with a thickness of 4 mm and an outer diameter of 24 mm (the maximum dimension normally used for medical instruments intended for rectal insertion). A 1.5 mm groove is cut in both inner surfaces to support the printed circuit board (PCB) on which the Timepix detectors are mounted. The shell includes a number of hollow cavities into which multiple captive spherical tungsten occluders may be fitted.

In this work, the performance of two alternative occluder configurations is evaluated, although many other configurations are possible. The choice of occluder locations is determined by the desired field of view and the specific location of the tumour. Each

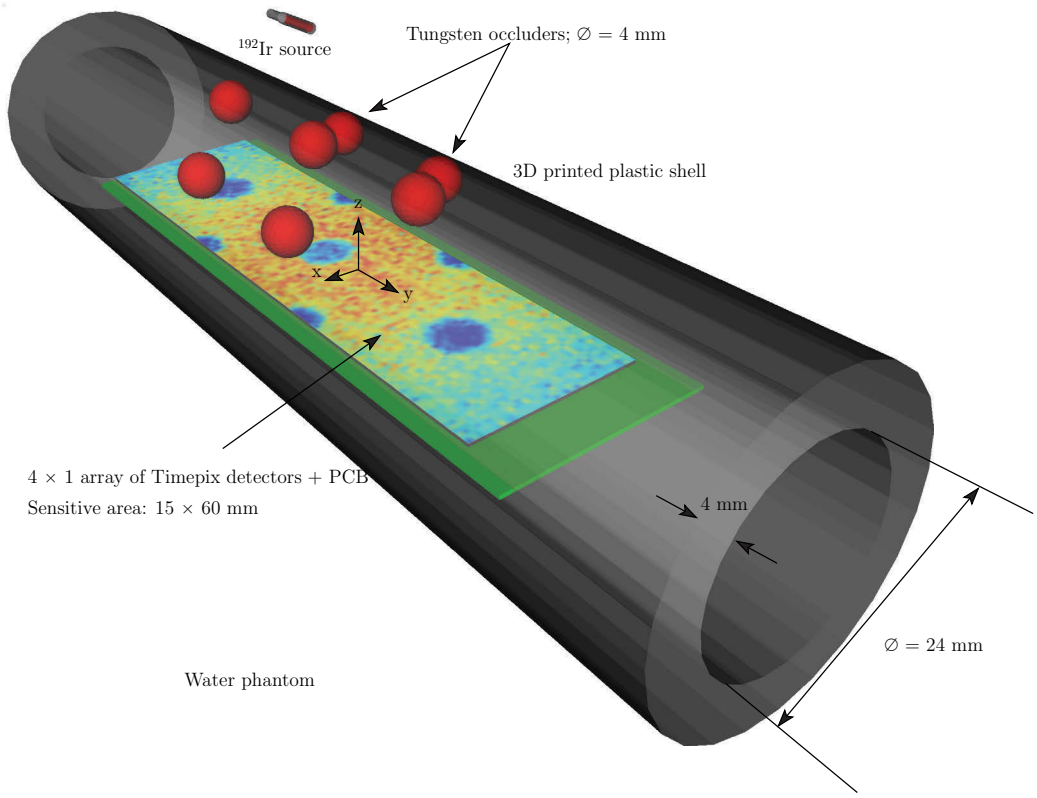

Figure 3.2: The BrachyShade probe with 7 occluders.

.

occluder is made from MT-18F tungsten alloy (95% W, 3.5% Ni, 1.5% Fe), which is available in the form of high-precision industrial ball bearings, and can be sourced in small quantities for a few dollars each in a variety of sizes. The two designs evaluated in this Thesis feature three and seven spherical occluders, each with a diameter of 4 mm (i.e. the same as the thickness of the cylindrical plastic shell. The diameter is not critical, however 4 mm tungsten spheres are commonly used as motor bearings and are readily available from many suppliers. In the three-occluder design, the spheres are arranged in a line parallel to the long axis of the detector, centred at a height 10 mm above the centre of the detector plane and directly above the midpoints of the joints between adjacent Timepix detectors (at axial displacements of -15, 0 and +15 mm). The field of view of the detector is defined as the wedge-shaped volume above the detector in which the source will project at least half a shadow onto the detector plane. A 3D rendering of the proposed designs is shown in Figure 3.1.

The seven-occluder alternative design, shown in Figure 3.2 adds two additional 4 mm occluders on either side. These are also embedded in the plastic shell, at a

distance of 10 mm from the central axis but rotated at 45° from the vertical. Along the probe axis, the axial displacement of these secondary occluders was ±7.5 mm (i.e. at the midpoints between the three central occluders). The seven-occluder design offers an increased field of view relative to the 3-occluder case; however, as with HDR BrachyView, it should is also possible to rotate the 3-occluder version of the probe in order to increase the field of view.

It is important to note that there is no specific restriction on the diameter of the spheres, nor their placement within the restrictions of the 24 mm plastic shell; placing the occluders closer to the detector plane will increase the field of view, however due to the 'minification' effects of the geometry of this situation, the spatial resolution of the probe will be reduced. The geometry as described in Figure 3.1 and 3.2 offers a good field of view, and enables imaging of the majority of the prostate volume.

3.2 Source Position Estimation Algorithm

The source position estimation algorithm is based on an analytic model of the expected pattern of photons which interact with the detector plane, given the source and occluder positions, which is described in detail in Section 3.3. From a starting point somewhere in the volume above the occluders, the analytic model is used to generate the expected detected photon distribution on the detector. The mean squared error between the detected photon map and the image acquired by the physical Timepix array is then iteratively minimised by adjusting the estimated source position using the Levenberg-Marquardt optimisation algorithm, until the algorithm converges or a maximum number of iterations is reached. Convergence is normally achieved in less than 100 iterations.

If the analytic model properly accounts for all physics of the device and its surroundings, the resulting coordinates should be a very good estimate of the source position, limited only by the signal-to-noise ratio (SNR) of the acquired image, which in turn depends on the acquisition time. In practice, the analytic model is imperfect; in particular, it does not account for the effects of Compton scatter in the medium. However, the effects of Compton scatter on the estimated source position are quite deterministic, and can be corrected using a simple empirically-derived error model, described in detail in Section 3.4.

The accuracy of fitting depends on both the signal to noise ratio of the acquired image (which in turn depends on the acquisition time and the proximity of the source)

and also the pixel dimensions. Increasing pixel dimensions both increases signal to noise ratio (as each pixel will detect a larger number of photons) and decreases the spatial resolution with which the photon distribution can be measured. The pixel pitch of TimePix is 55 μm, which is much higher than needed for this application; therefore, it is possible to improve the signal to noise ratio without degrading overall accuracy by rebinning pixels into larger groups. This has the added benefit of significantly increasing the speed of the fitting process, since it greatly reduces the number of calculations needed during the optimisation process. For a realistic exposure interval of 100 ms, with a typical source activity of 370 GBq, rebinning in both x and y by a factor of either 4 or 8 resulted in the best overall performance (approximately the same in both cases). This provides a 16-fold or 64-fold reduction in the number of pixels in the image, greatly accelerating the fitting process.

3.3 Analytic Model

The model uses a right-handed coordinate system with its origin located at the physical centre of the sensitive volume of the detector array, as shown in Figure 3.1. The source is assumed to be an ^{192}Ir point source located at position $P_s = (x_s, y_s, z_s)$; the occluders are placed at $O_k = (0, y_{o,k}, z_o)$ mm, $k \in [1, 2, 3]$. Photons emitted from this source are subject to a number of possible sources of attenuation and Compton scattering; firstly, the photon path intersects with a volume of water (or approximately water-equivalent tissue); secondly, it may traverse a maximum of one tungsten-alloy sphere (it is possible for the photon path to intersect with more than one only if the source is located outside of the prostate volume); finally, any detectable photon will pass through the plastic shell (which is approximately tissue-equivalent) and a small volume of air in the void above the detector, before reaching the detector plane. Photons arriving at the detector may or may not be detected, with the probability of detection dependent on the energy of the photon and the angle of arrival. The Timepix is operated in count mode, with a conservative energy threshold of 16 keV.

To estimate the distribution of photons which would be detected for a given source location, a map of the gamma photon intensity which would arrive at the detector in the absence of media between the source and the detector is generated. At a distance d from a source emitting N photons of a particular wavelength per unit time, the flux density $\phi(d)$ at distance d will be

$$\phi(d) = \frac{N}{4\pi d^2}$$

photons per unit time per unit area. At a point $P_d = (x_d, y_d, 0)$ on the detector plane, $d = \sqrt{(x_d - x_s)^2 + (y_d - y_s)^2 + z_s^2}$. Furthermore, the angle between the normal of an infinitesimal area dA centred at $(x_d, y_d, 0)$ on the detector plane to the line joining it to the source position is given by $\sin^{-1}\left(z_s/\sqrt{(x_d - x_s)^2 + (y_d - y_s)^2 + z_s^2}\right)$; therefore, the flux density at the surface, based on free-space path loss only, will be:

$$\begin{aligned}\phi_{fs}(x_d, y_d) &= \frac{N}{4\pi((x_d - x_s)^2 + (y_d - y_s)^2 + z_s^2)} \times \\ &\quad \frac{z_s}{\sqrt{(x_d - x_s)^2 + (y_d - y_s)^2 + z_s^2}} \\ &= \frac{N z_s}{4\pi((x_d - x_s)^2 + (y_d - y_s)^2 + z_s^2)^{\frac{3}{2}}}\end{aligned}$$

The path length through water can be calculated by finding the distance from the source to the point of intersection between the line from P_d to P_s and the inner surface of the cylinder. The cylinder itself is assumed to be water-equivalent. We assume that water only attenuates incident gamma photons and do not attempt to model Compton scattering. This assumption is not valid in practice; however, analytic modelling of Compton scatter is difficult and computationally expensive, since in order to determine the effect of scatter on the shadows, the angle of arrival would need to be computed for each photon, negating the value of an analytic model. Instead, we ignore scattering at this stage an apply an empirical correction factor at a later stage of the process of determining source location.

The equation of the line joining P_d and P_s is:

$$\begin{bmatrix} x \\ y \\ z \end{bmatrix} = \begin{bmatrix} x_d \\ y_d \\ 0 \end{bmatrix} + t \begin{bmatrix} l_x \\ l_y \\ l_z \end{bmatrix} \tag{3.1}$$

where t is the distance along this line from P_d, $l_x = (x_s - x_d)/d$, $l_y = (y_s - y_d)/d$, $l_z = z_s/d$ and $d = \sqrt{(x_s - x_d)^2 + (y_s - y_d)^2 + z_s^2}$. Solving for the point of intersection between this line and the inner surface of the cylinder (with radius R_c) reduces to finding the point of intersection between the upper half of a circle of radius R_c and

the projection of the previously-mentioned line on the xz plane, since the cylinder is parallel to the y axis:

$$R_c^2 = (x_d + tl_x)^2 + (tl_z)^2$$

Re-arranging to solve for parameter t (for the positive semicircle only, i.e. the upper half-cylinder):

$$t = -\frac{x_d l_x + \sqrt{x_d^2 l_x^2 - (l_x^2 + l_z^2)(x_d^2 - R_c^2)}}{l_x^2 + l_z^2}$$

This parameter can be substituted back into (3.1) to solve for the coordinates of the point of intersection, which allows the distance through water by a photon emitted by the source arriving at the detector plane to be calculated, and hence the probability that this photon will be absorbed or transmitted through that space:

$$\begin{aligned} p_x &= x_d + tl_x \\ p_y &= y_d + tl_y \\ p_z &= z_d l_z \\ d_{H_2O} &= \sqrt{(p_x - x_s)^2 + (p_y - y_s)^2 + (p_z - z_s)^2} \end{aligned} \tag{3.2}$$

For each of the k tungsten-alloy occluders, (3.1) can be solved simultaneously with the equation of a sphere of radius R_o centred at O_k. This results in a quadratic equation, with the discriminant:

$$\begin{aligned} \Delta = &((x_s - x_d)x_d + (y_s - y_d)(y_d - y_s) - z_s z_o)^2 \\ &- (x_d.^2 + (y_d - y_s).^2 + z_o.^2) + R_o^2 \end{aligned} \tag{3.3}$$

If this discriminant is positive, the line from the detector plane to the source intersects with the tungsten-alloy sphere. Therefore, the total path length through the occluder is:

$$d_W = \begin{cases} 2\sqrt{\Delta} & \Delta > 0 \\ 0 & \Delta \leq 0 \end{cases}$$

The path length through the occluder, if any, is also subtracted from the path length through water. The number of photons of wavelength λ_i per unit time per unit area arriving at the surface of the detector are then:

$$\phi_{arr}(x_d, y_d) = \phi_{fs}(x_d, y_d) e^{-\mu_{H_2O}(\lambda_i)(d_{H_2O} - d_W)} e^{-\mu_W(\lambda_i) d_W}$$

where $\mu_{H_2O}(\lambda_i)$ and $\mu_W(\lambda_i)$ are the linear attenuation coefficients of water and tungsten alloy at wavelength λ_i, respectively. The number of photons which deposit some energy during their interaction with the detector (either photoelectrically or, more frequently, through Compton scattering) per unit time per unit area depends on the thickness of silicon through which they pass, which in turn depends on the angle of arrival - a simple function of the relative position of the source and the point on the detector and the thickness of the detector, t_{det}. To simplify the analytic model, we ignore the fact that the path from the source to a given pixel on the detector may intersect with more than one pixel, and assign the totality of interaction probability to the pixel centred at (x_d, y_d):

$$\phi_{det}(x_d, y_d) \approx \phi_{arr} \left(1 - e^{-\frac{d}{z_s} t_{det} \mu_{Si}(\lambda_i)}\right)$$

To generate a good approximation of the expected map of detected photons for a given source position (x_S, y_s, z_s), then, the area of the detector is quantised into individual pixels (in the case of the Timepix detector, these pixels are each 55 μm $\times$ 55 μm in size), ϕ_{det} is calculated at the centre of each pixel for each wavelength present in the source spectrum, multiplied by the area of the pixel and the duration of the observation; the total count is summed by weights corresponding to the relative distribution of wavelengths in the source spectrum.

3.4 Compton Scatter Correction

While the analytic model described in Section 3.3 provides a good estimate of the shadow map in the absence of a scattering medium, the probe is intended for use inside the human body, where Compton scattering is a significant factor. The effect of Compton scattering is to reduce the contrast of the illuminated and shadowed regions, since some photons can 'go around' the occluders via Compton scattering. The discrepancy between the physical process and the analytic model has a relatively small impact on the accuracy of the estimate of the position in the x and y dimension;

however, it results in a significant overestimate (of the order of 10%) of the source position in the z dimension. Analytic modelling of the three-dimensional distribution of photon paths from a point source in a Compton-scattering medium is complex; most published models for Compton scatter only attempt to estimate spectra or dose distribution on a plane for a point source in a uniform medium (i.e., without the presence of occluding objects).

Instead, in this work, an empirical model is used to model and correct the effects of Compton scatter on the estimated source position. Defining the volume of interest as a 40 mm×40 mm×40 mm cube centred at $(0, 0, 40)$ mm, it may be observed that both BrachyShade and volume of interest (VoI) are symmetric about both the xz and yz planes. Therefore, a model developed for correcting the error in the positive xy quadrant of the VoI, $(0 \leq x \leq 20, 0 \leq y \leq 20, 20 \leq z \leq 50)$, can be applied to the other quadrants by symmetry. A 9×9×9 lattice is constructed within this volume, with points spaced by 2.5 mm in x and y and 5 mm in z. Therefore, a total of 729 Geant4 (version 10.3p2) simulations were conducted, with a simulated ^{192}Ir point source placed at each of these locations. A total of 5 billion primaries were simulated; the acquired images were then used together with the fitting algorithm to estimate the source locations for each point, and the error vector between the ground truth location and the estimated source positions calculated.

Two distinct classes of error vectors are observed. The first, and most useful in this work, is the set of error vectors at points for which most or all of the shadows are projected onto the detector surface, corresponding to a wedge-shaped region parallel to the y axis. In this region, R_1, the error vectors point approximately towards the origin of the coordinate system, and have a magnitude of the order 10% of the distance from the origin; the magnitude and direction of the error vector field varies smoothly as a function of position. The second class is the set of which do not project shadow on the detector plane; these still encode some information in the detected-photon distribution, but with much less specificity as there is little structure in the image. This region is denoted R_2. There is also a small intermediate region, R_i for which the shadow is partially on the detector plane.

Of these regions, the first is of the greatest interest, since it corresponds to the bulk of the prostate volume; furthermore, like HDR BrachyView, if the FoV is insufficient to observe the entire treatment volume directly, it is possible to rotate the imaging system around its y axis relative to its (stationary) outer shell to achieve the desired coverage. In this region, the smoothly varying error vector field can be approximated well as a

polynomial function of estimated source position. The model has been implemented with a linear, second-order (quadratic) and third-order model. In most cases, the quadratic model performs better than the linear model, and the third-order model performs no better than the quadratic. The exception to this is the error vector field generated by the alternative position estimation algorithm (introduced in Section 3.5; in this case, a third-order polynomial model was found to be a superior option.

While it is possible to express this error field as a function of *true* source position, which makes more intuitive sense, expressing it as a function of *estimated* source position allows the error to be conveniently corrected. The problem, then, becomes one of determining the coefficients $a_{x|y|z,\{1-7\}}$ (for the quadratic error mode - each component has three additional terms for the third-order polynomial variant), which, given the estimated position $(\hat{x}, \hat{y}, \hat{z})$, allow the error to be determined and hence corrected:

$$\begin{aligned} e_x &= a_{x,1}\hat{x}^2 + a_{x,2}\hat{x} + a_{x,3}\hat{y}^2 + a_{x,4}\hat{y} + a_{x,5}\hat{z}^2 + a_{x,6}\hat{z} + a_{x,7} \\ e_y &= a_{y,1}\hat{x}^2 + a_{y,2}\hat{x} + a_{y,3}\hat{y}^2 + a_{y,4}\hat{y} + a_{y,5}\hat{z}^2 + a_{y,6}\hat{z} + a_{y,7} \\ e_z &= a_{z,1}\hat{x}^2 + a_{z,2}\hat{x} + a_{z,3}\hat{y}^2 + a_{z,4}\hat{y} + a_{z,5}\hat{z}^2 + a_{z,6}\hat{z} + a_{z,7} \end{aligned} \tag{3.4}$$

The coefficients $a_{x|y|z,\{1-7\}}$ may be calculated by constructing an system of linear equations from the estimated source positions and calculated errors within R_1, and determining the least-squares fit. An exact solution cannot be obtained, since each observation of the error is noisy (due to the statistical noise inherent in the simulation); however, the large number of points available allow a good estimate of the coefficients to be obtained, which are the best fit for the overall set of observations.

Given a set of N points inside the first region, let

$$\mathbf{E}_{x|y|z} = \begin{bmatrix} e_{x|y|z}(1) \\ e_{x|y|z}(2) \\ e_{x|y|z}(3) \\ \dots \\ e_{x|y|z}(N) \end{bmatrix}$$

where $e_{x|y|z}(k)$ is the error component in x, y or z for the kth point in the first region, $k \in [1, 2, \dots, N]$. Now, defining

$$\mathbf{P} = \begin{bmatrix} \hat{x}(1)^2 & \hat{x}(1) & \hat{y}(1)^2 & \hat{y}(1) & \hat{z}(1)^2 & \hat{z}(1) & 1 \\ \hat{x}(2)^2 & \hat{x}(2) & \hat{y}(2)^2 & \hat{y}(2) & \hat{z}(2)^2 & \hat{z}(2) & 1 \\ \hat{x}(3)^2 & \hat{x}(3) & \hat{y}(3)^2 & \hat{y}(3) & \hat{z}(3)^2 & \hat{z}(3) & 1 \\ \dots & & & & & & \\ \hat{x}(N)^2 & \hat{x}(N) & \hat{y}(N)^2 & \hat{y}(N) & \hat{z}(N)^2 & \hat{z}(N) & 1 \end{bmatrix}$$

and

$$\mathbf{A}_{x|y|z} = \begin{bmatrix} a_{x|y|z,1} \\ a_{x|y|z,2} \\ a_{x|y|z,3} \\ a_{x|y|z,4} \\ a_{x|y|z,5} \\ a_{x|y|z,6} \\ a_{x|y|z,7} \end{bmatrix}$$

(3.4) may be expressed in matrix form and solved by inverting $\mathbf{P}$ to determine $\mathbf{A}_{x|y|z}$:

$$\mathbf{E}_{x|y|z} = \mathbf{P}\mathbf{A}_{x|y|z}$$
$$\mathbf{P}^{-1}\mathbf{E}_{x|y|z} = \mathbf{P}^{-1}\mathbf{P}\mathbf{A}_{x|y|z} = \mathbf{A}_{x|y|z}$$

Since $\mathbf{P}$ is not square (the number of rows exceeds number of columns), the Moore-Penrose pseudoinverse $\mathbf{P}^{+}$ is used, calculated via singular value decomposition (SVD). The resulting coefficients $\mathbf{A}_{\mathbf{x|y|z}}$ for the x, y and z components, respectively, may then be used, together with the estimated source location returned by the position-estimation algorithm, to provide an estimate of the error in the source location, which simply be added to the estimated source location to provide an improved estimate $(\hat{x}', \hat{y}', \hat{z}')$ for any point inside R_1.

3.5 An Alternative Source Localisation Algorithm: Hierarchical Pattern Matching

An alternative method for source localisation has also been proposed, implemented and evaluated for a limited number of source locations. The basic principle is to construct a

3D array of 2D images, each of which is the image computed using the analytic model for a given point in the volume of interest above the detector plane. The volume is quantised in each dimension at a particular resolution (for example, 0.5 mm); 4-way symmetry is again exploited to minimise the memory storage requirements (noting that the detector is symmetric both along its long and short axis).

A fast search is performed at low spatial resolution (for example, in quantisation steps of $Q_0 = 5$ mm in each dimension), in which the test image (i.e. the acquired or simulated detected photon map) is compared to each of the images in the reference image library using one of a number of possible metrics. The index corresponding to the image which yields the best match corresponds to the coordinates of a first-order approximation of the source location. Now, the sub-region centred at this location and extending $\pm Q_0$ in each dimension is searched at high resolution (for example $Q_1 = 0.5$ mm); again, the index corresponding to the image which results in the best match is identified, with the corresponding coordinates being the source position estimated at the maximum spatial resolution. If desired, this hierarchical image matching method could be extended to a third level; however, in practice, the algorithm is sufficiently fast so as to not require a 3-level search.

The choice of the most appropriate image metric is an interesting one. Classical image similarity metrics such as mean squared error are not ideal for this application, since they give equal value to pixels belonging to the background of the image (which encode little spatial information) and pixels belonging to the shadow region (which encode much more significant spatial information). Worse, the shadow region is more severely affected by Compton scatter; the shadow region is always made brighter than it would be in the absence of Compton scatter, while background regions are roughly equally likely to have 'lost' photons (scattered away from the direct path from the radiation source) as to have 'gained' photons scattered from elsewhere. Therefore, Compton scatter disproportionately degrades the quality of information present in the shadow compared to the equally-weighted (per-pixel) background.

While it is possible to correct for scatter in the same way as the error-minimisation algorithm proposed in Section 3.2, it is also possible to use a different metric which significantly reduces the impact of this problem. One such metric is the structural similarity index measure (SSIM), which is intended to model human perceptual image response characteristics in comparing the similarity of two images; it tends to put a heavier emphasis on the similarity of *shapes* rather than on the magnitude of differences in intensity between images [81]. There may be other image metrics which perform

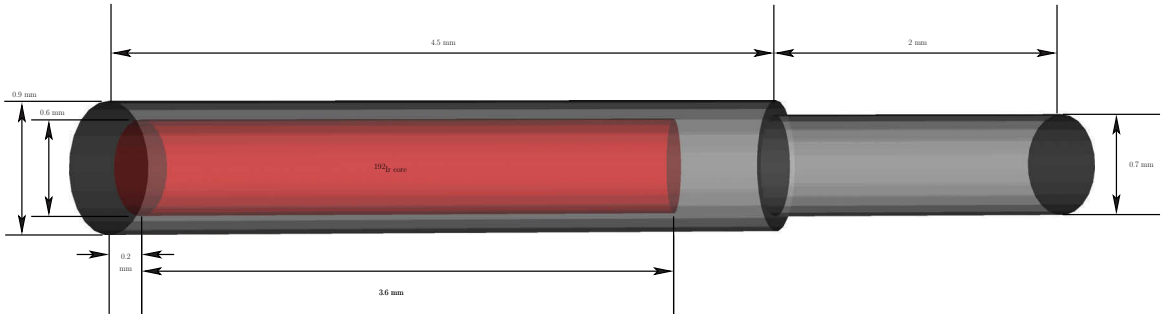

Figure 3.3: The simulated ^{192}Ir HDR brachytherapy source. The core consists of pure iridium with a uniform distribution of ^{192}Ir, surrounded by a steel shell [82, 83].

even better in this application; this question remains open and will be the subject of further work in the immediate future.

3.6 Monte Carlo simulations

3.6.1 Simulation Framework, Models and Parameters

Simulations were performed using Geant4 10.3p2. Electromagnetic interactions were modelled using the Livermore Low Energy physics package, with cuts of 1 μm in the target region and 4 mm in the phantom region, for all gamma, electron and positron interactions. For scatter correction, each source position was simulated with 5 billion decays. For a typical source activity of 370 GBq, this corresponds to an acquisition period of 13.5 ms. True radioactive decay is not modelled; instead, photons are emitted from uniformly distributed random locations within the active region of the source model, in a uniformly distributed random direction, with the proportions of each photon energy determined according to the ^{192}Ir spectrum (see Table 3.1). This provides a realistic model for the spectrum of the real source, regardless of the age of the source, since ^{192}Ir decays directly into stable ^{192}Pt, with no other radioactive species produced. In the real source, all β^- radiation is blocked by the steel shell (see Figure 3.3).

3.6.2 Source Model

The model source used in this work is the iridium-192 MicroSelectron-HDR, described by Borg et al. and Daskalov et al. [82, 84]. The core consists of a pure iridium metal cylinder, 3.6 mm long and 0.6 mm in diameter, with ^{192}Ir uniformly distributed throughout the volume. This is surrounded by a steel shell, 4.5 mm long and 0.9 mm

Table 3.1: ^{192}Ir gamma spectrum [82]

Energy (keV)	Emitted Fraction (%)
10.5	2.45
64	4.54
75	1.22
136.5	0.0766
201.5	0.205
205.5	1.41
283.5	0.113
295.5	12.2
308.5	11.4
316.5	36.3
374.5	0.305
416.5	0.281
468.5	20.2
484.5	1.34
489.5	0.181
588.5	1.90
604.5	3.45
612.5	2.23
884.5	0.107

in diameter, which is connected to a short steel cable (2 mm long and 0.7 mm in diameter). A schematic of the source is shown in Figure 3.3

The spectrum of the simulated ^{192}Ir source is shown in Table 3.1.

3.6.3 Planned Simulations and Analysis

The basic design objective is to be able to track the source with sub-millimetre accuracy within the prostate volume. A diseased prostate may have a volume of between 30 and 60 mL [31]. If the prostate is assumed to be roughly spherical, this would correspond to a sphere with a diameter of approximately 48 mm in the most extreme case, whereas if assumed to be cubic, the sides would be approximately 39 mm in length. In practice, it is a somewhat irregular shape; therefore, for simplicity, in this work it is assumed that the prostate is entirely contained within a cubic volume in a volume of 40 mm×40 mm×40 mm, which would be sufficient to enclose the majority of cases.

The specific simulations that are to be performed will be described in the following sections.

3.6.3.1 Compton Scatter Evaluation

To evaluate the effects of scatter on photons of different energies, and validate the detection efficiency and photon transport model used for the analytic model of the photon/shadow map, a simulation will be conducted with no occluders, with the (real) source placed at distances of between 10 mm and 75 mm above the centre of the detector. For each of the photon energies present in the spectrum listed in Table 3.1, the average number of photons detected in a cluster of four pixels immediately under the centre of mass of the source will be measured as a function of distance. The simulation will be conducted firstly without a scattering medium, which is expected to be in close alignment with the analytic model; and secondly, with the scattering medium (water) present between the source and the detector.

3.6.3.2 Source Position Estimation Results Prior to Compton Scatter Correction

The source will be moved through each point on a 9×9×9 grid (a total of 729 points) located in one quarter of the 40 mm×40 mm×40 mm prostate volume (from 0 to 20 mm in x and y in steps of 2.5 mm and from 0 to 40 mm in z in steps of 5 mm), since by symmetry the results can easily be extended to the other three quadrants. In each position, five billion primary decays will be simulated according to the spectrum listed in 3.1, with both the 3-occluder and 7-occluder probe.

The true locations for each simulation will be combined with the estimated locations resulting from uncorrected result in order to generate the coefficients for the correction matrix.

3.6.3.3 Results After Compton Scatter Correction

The correction matrix generated will be applied to the uncorrected position estimates, and the residual error calculated for both probes. The residual error will also be plotted as a function of distance from the centre of the detector.

3.6.4 Fast Hierarchical Pattern Matching

Preliminary position estimates computed using the alternative Fast Hierarchical Pattern Matching algorithm will be evaluated at a limited number of points and compared to the error-minimisation algorithm applied to the same data;

3.7 Conclusion

This Chapter introduced the proposed probe design, and described a complete source location estimation algorithm based on error-minimisation between an analytic model and the observed photon maps, featuring an empirically-derived post-processing technique for Compton scatter correction. An alternative algorithm based on an efficient hierarchical pattern matching technique was also introduced; results obtained for a limited number of test locations are also presented in Chapter 4. Finally, the means by which the data for the Compton scatter correction algorithm will be prepared and the simulation scenario to be used to evaluate the performance of the system are described; the results are presented in Chapter 4.

CHAPTER 4

Results and Discussion

This chapter presents Monte Carlo simulation results for both variants of the proposed design. Section 4.1 describes a simple Monte Carlo evaluation of the effects of Compton scatter at different energies. Section 4.2 presents the raw results for positioning error obtained for the three-occluder and seven-occluder configurations with no Compton scatter correction applied, evaluated at 729 locations in one-quarter of the field of view of the device. Section 4.3 presents corresponding results with the scatter correction applied, demonstrating the efficacy of the correction algorithm. Section 4.4 presents some limited simulation results for the proposed alternative method based on fast hierarchical pattern matching. The implications of all results, together with some concluding remarks, are discussed in Section 4.5.

4.1 Compton Scatter Evaluation and Analytic Model Validation

To validate the correctness of the analytic model (which does not account for scattering), quantify the effect of Compton scattering and determine whether or not correction is needed, a series of Monte Carlo simulations was performed for a point source at a varying distance to the detector, with no occluders present. The source is located directly above the centre of the detector, and moved from an altitude of 10 mm to 75 mm

above the surface of the detector, in increments of 1 mm. The probe is as described in Chapter 3; two sets of simulations are conducted, one with the water phantom, and a second with the water phantom replaced by a vacuum (thereby removing the effects of scattering). The analytic model is then run with the same simulation scenario, with attenuation due to water turned off (as the analytic model does not account for scattering, only attenuation). Detection sensitivity, which is a function of both geometry, medium attenuation, detector material and thickness and Compton scatter in the medium, is measured by calculating the average fraction of the total emitted photons which is detected per pixel for the cluster of four pixels immediately under the centre of mass of the source (or the point source, for the case of the analytic model).

Figure 4.1 shows sensitivity plotted against $1/d^2$, where d is the distance directly above the centre of the detector plane, for the four most significant source energies present in the spectrum (namely 295.5 keV, 308.5 keV, 316.5 keV and 468.5 keV), for the simulation without scatter, simulation with scatter and analytic model. The simulation without scattering medium (Figure 4.1(a)) is evidently in strong agreement with the the results from the analytic model (Figure 4.1(c)). The small differences in response are exaggerated when plotted against $1/d^2$. The relative sensitivity of the detector to each energy is very similar, with lower sensitivity to the highest energy (since high-energy photons are more penetrating than low-energy photons). Additionally, the plot is essentially linear, indicating that sensitivity is directly proportional to $1/d^2$ as expected in the absence of scatter. By contrast, low-energy photons are more susceptible to Compton scattering; therefore, when a scattering medium is introduced, the detector is more sensitive to the highest energy than the lowest. This is the reason that the order of the curves is reversed when the source is placed in the scattering medium. The relationship with $1/d^2$ is also somewhat less than linear for all energies when scattering is present.

Since the scatter-free simulation is in close agreement with the simulation when scattering is included, this experiment confirms that the analytic model is correct as far as it goes; however, it is clearly essential to deal with the problem of scattering, as this causes a significant deviation between the analytic model and the observed photon map.

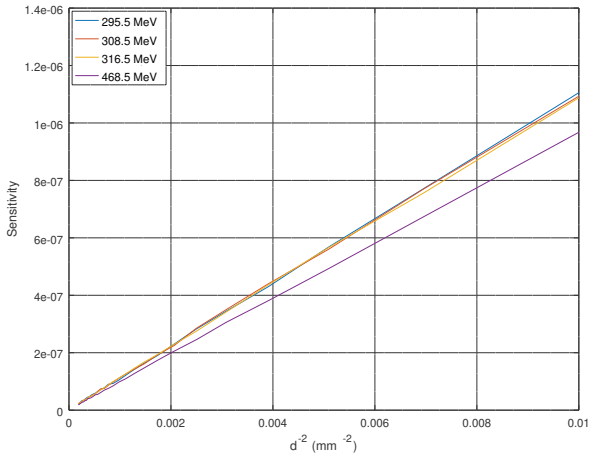

(a) Monte Carlo simulation, no scattering medium present

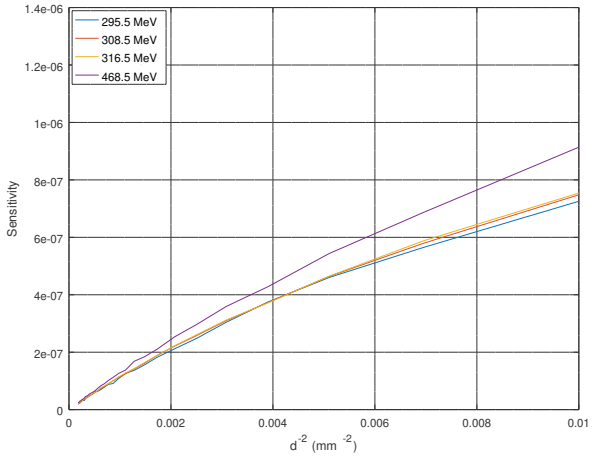

(b) Monte Carlo simulation, scattering medium present (water)

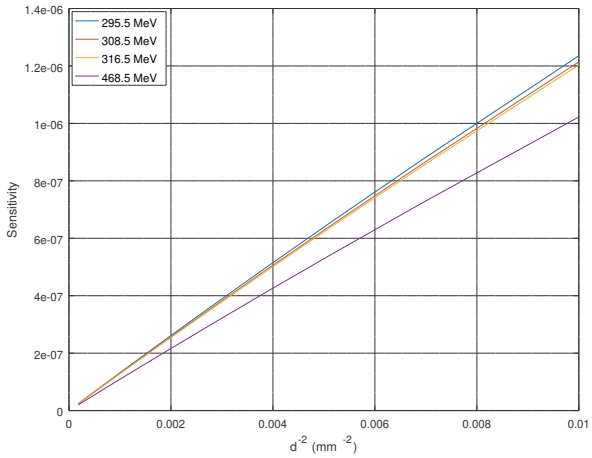

(c) Analytic model (ignoring effects of scattering)

Figure 4.1: Sensitivity as a function of depth for Monte Carlo simulations with and without the presence of a scattering medium, and for the analytic model, showing the most four significant source energies.

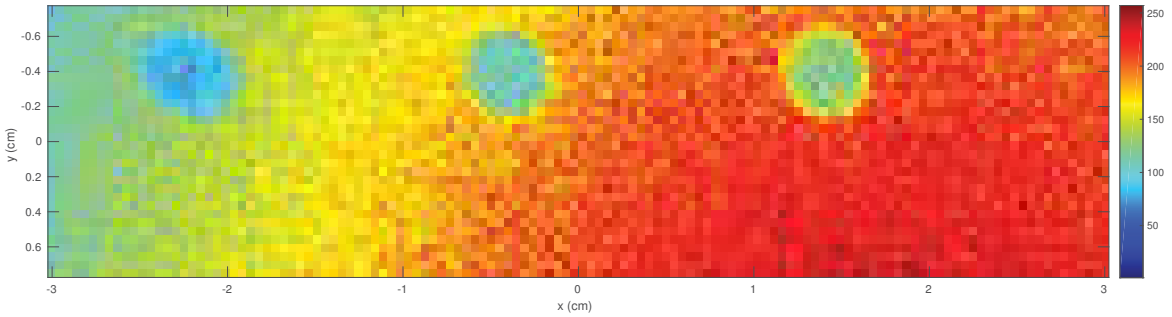

(a) Simulation data

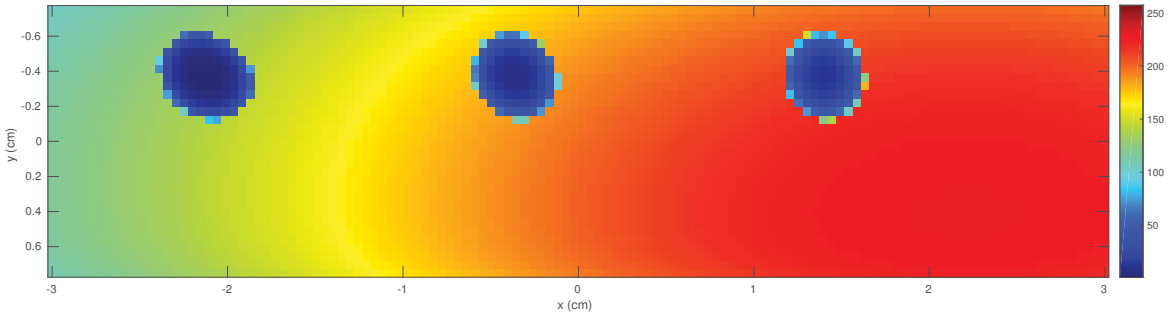

(b) Analytic fit

Figure 4.2: Example of raw output from Geant4 simulations (37×10^9 primary particles, real ^{192}Ir source model centred at (18.5, 20, 60) mm), with the results of the fitting process. Without Compton scatter correction, the fitting algorithm estimates the location as being (22.0, 21.9, 70.8) mm.

4.2 Uncorrected Position Estimation Results

Figure 4.2 shows an example of simulation output and corresponding results from the fitting process. A significant and systemic error is evident; each component of the source position is overestimated, with the biggest error being in the z dimension. The reason for this is obvious upon comparison of Figures 4.2(a) and 4.2(b) - the contrast between the shadow region and the directly illuminated part of the detector is much less in the simulation compared than in the analytic model, because the analytic model does not account for Compton scattering. This results in some radiation being scattered around the occluder, illuminating parts of the detector which would be in shadow if it were not for the scattered photons. Figure 4.3 shows the simulation and analytic images for a common location in space, together with a representation of the source model (for the simulation); the main obvious difference is the contrast between shadowed and unshadowed regions. Despite this difference, the *shape* of the images is very similar; this is significant for the second position estimation algorithm whose results are presented in Section 4.4.

4.3 Compton Scatter Correction

4.3.1 Results from probe design with 3 occluders; Restricted FoV

Figure 4.4 shows the error at each of points in one quarter of the FoV as a vector field (error vectors are shown at the same scale as the spatial dimensions in the figure). While a simulation has been performed evaluated at all 729 points in the rectangular 20 mm $\times$ 20 mm $\times$ 40 mm volume, only points which are within the full field of view, defined as the vertically-oriented wedge within which a source cast at least half a shadow on the detector, are included in the fitting process; the error field takes quite a different character beyond this point, as there is insufficient structural information for the optimisation algorithm to lock on to (as will be seen in Section 4.3.2).

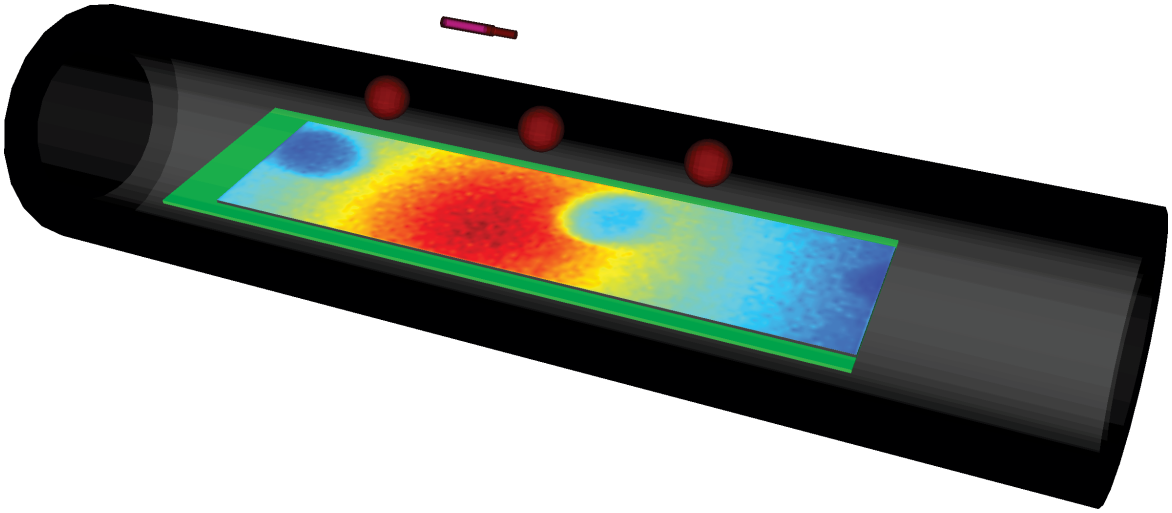

(a) Geant4 simulation (full source model)

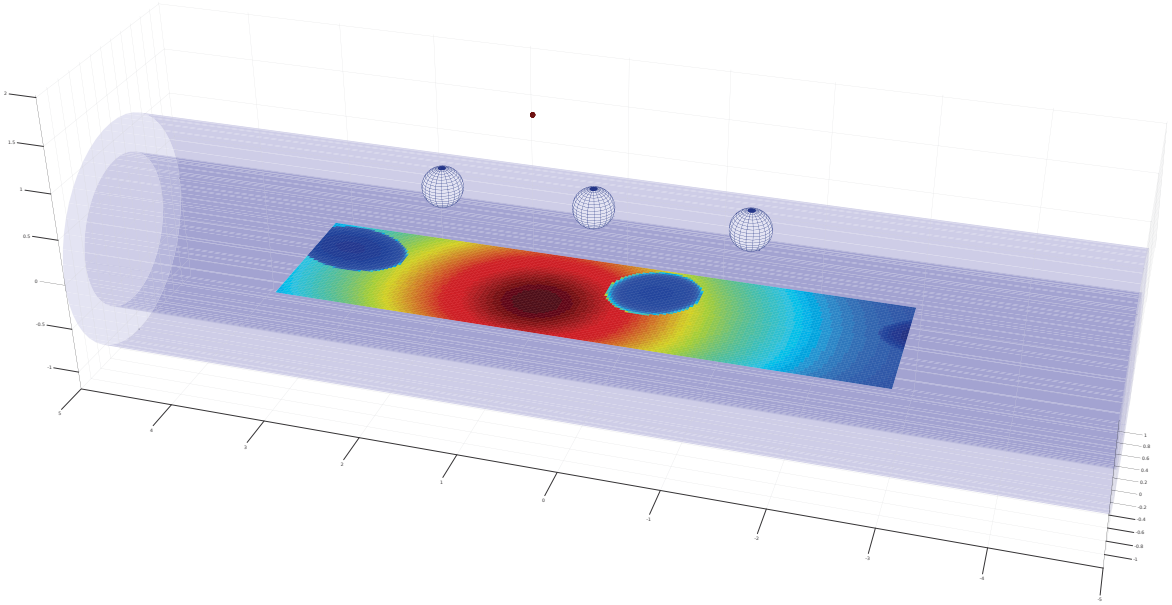

(b) Analytic model (point source)

Figure 4.3: Comparison of simulation output and analytic model for source located at (2.5, 5, 20) mm.

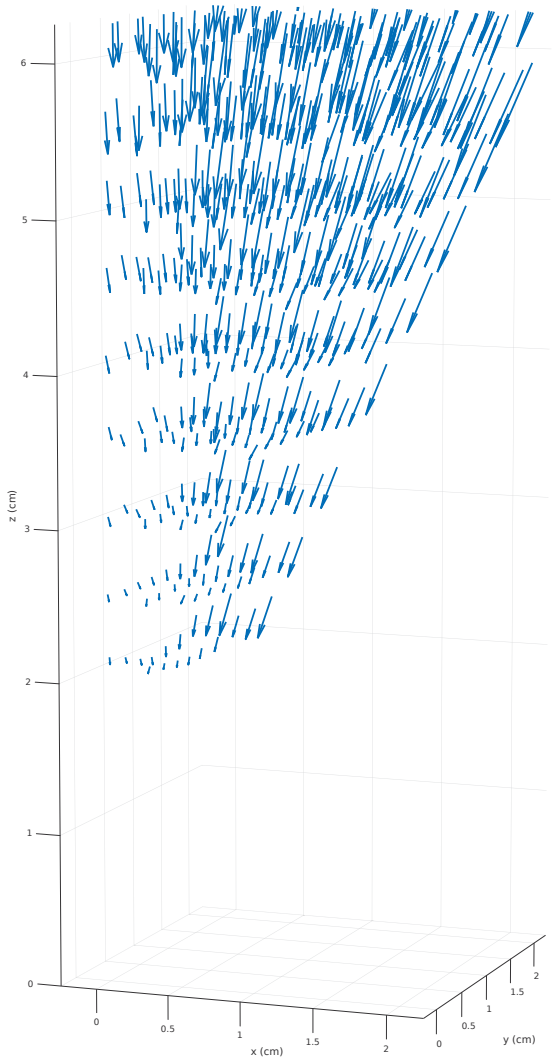

Figure 4.4: Uncorrected error vector field for 3-occluder system as a function of estimated source position.

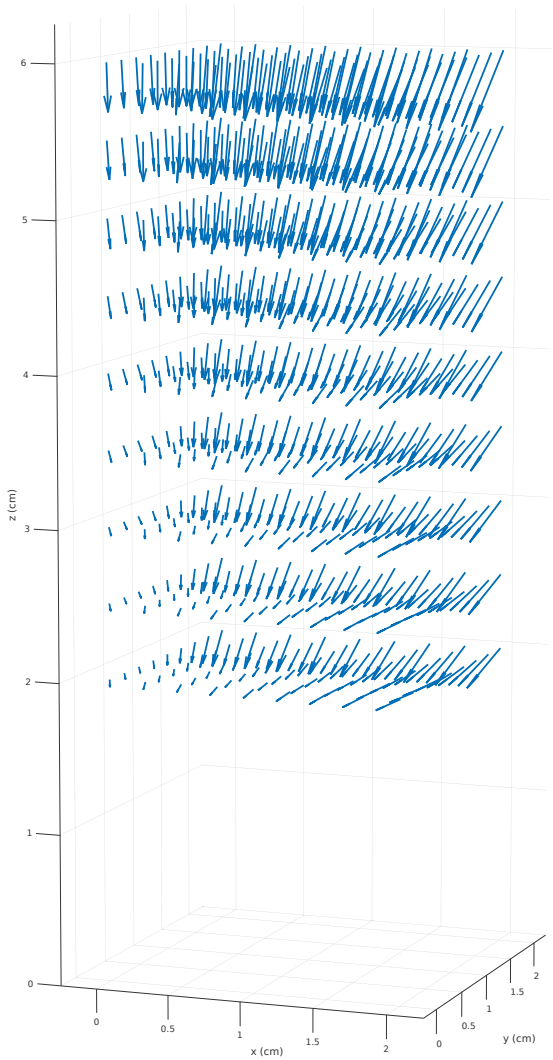

Figure 4.5: Compton-scatter error correction vector field for 3-occluder system, shown as a function of estimated source position. The field is a 3D second-order polynomial fitted to the raw error vector field.

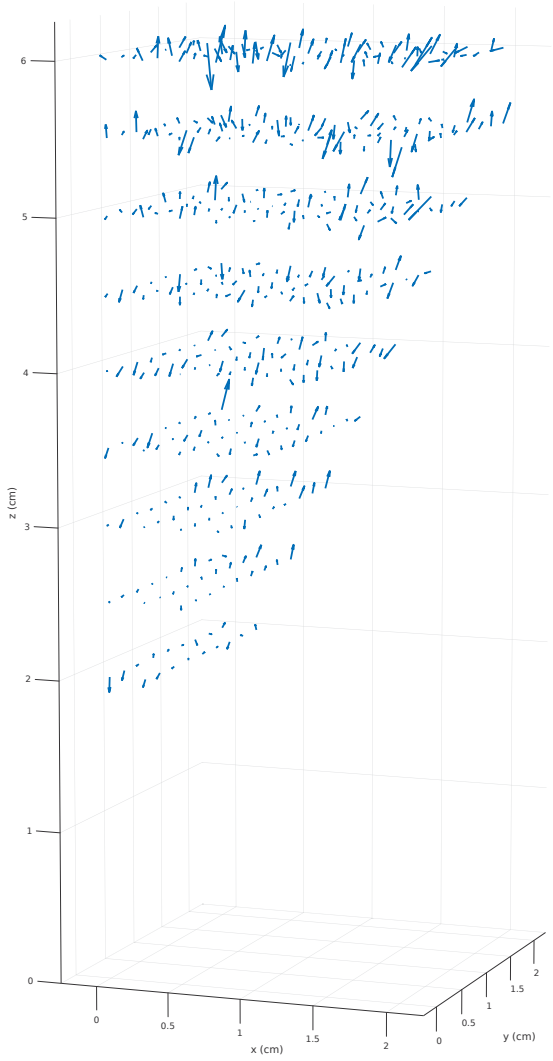

Figure 4.6: Residual error after correction added to original position estimate.

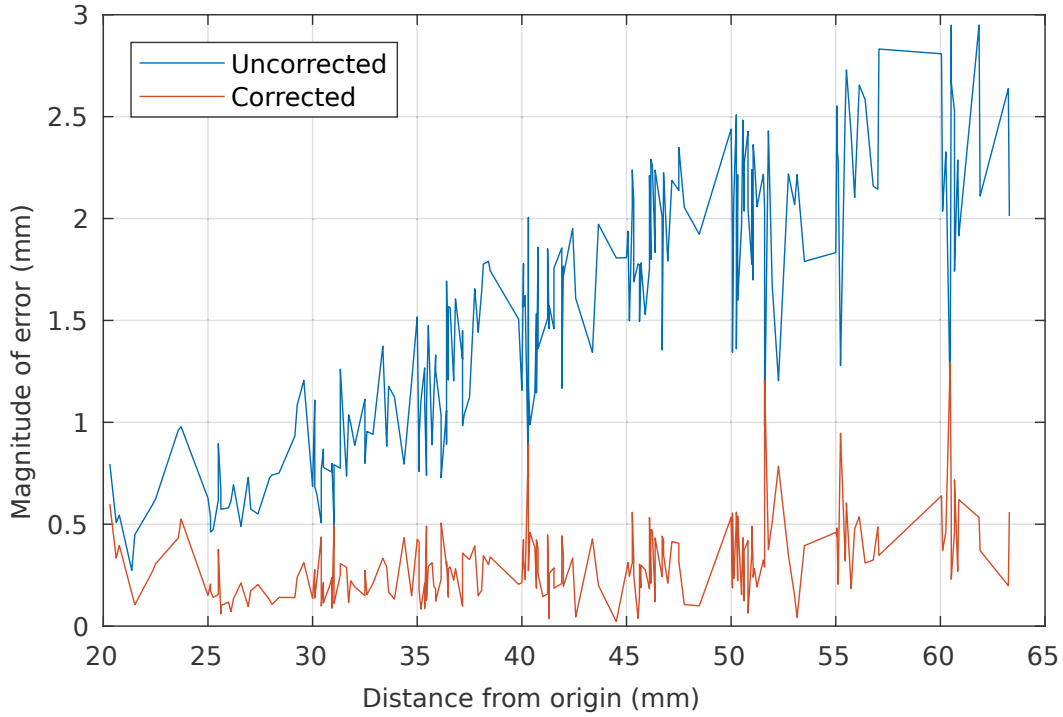

Figure 4.7: Error as a function of distance from (0, 0, 0), before and after applying the Compton scatter correction field.

The fitted second-error polynomial model of the error field is shown in Figure 4.5, evaluated at all points in this volume. The coefficients are as shown in (4.1):

$$\mathbf{A}_x = \begin{bmatrix} 0.0065 \\ -0.0605 \\ -0.0042 \\ 0.0019 \\ -0.0002 \\ 0.0031 \\ 0.0003 \end{bmatrix} ; \ \mathbf{A}_y = \begin{bmatrix} 0.0014 \\ -0.0032 \\ -0.0109 \\ 0.0045 \\ 0.0015 \\ -0.0125 \\ 0.0269 \end{bmatrix} ; \ \mathbf{A}_z = \begin{bmatrix} -0.0003 \\ -0.0033 \\ -0.0046 \\ -0.0161 \\ 0.0017 \\ -0.0653 \\ 0.1031 \end{bmatrix} \tag{4.1}$$

After subtracting the estimated error from the uncorrected source position estimates, the residual error field is as shown in Figure 4.6. The residual error is essentially random; it is no longer biased and it gradually increases with distance from centre of the detector plane (i.e. the origin of the coordinate system). This error is essentially limited by the signal to noise ratio (SNR) of the acquired image. In practice, acquisition times would be expected to be at least 100 ms, which is expected to greatly reduce the maximum error in position estimation.

Table 4.1: Residual error prior to Compton scatter correction

	Residual Error (mm)
Minimum	0.3334
1st quartile	1.0485
Median	1.4611
3rd quartile	1.9405
Maximum	3.0742

Table 4.2: Residual error after Compton scatter correction; with an accurate model of an HDR brachytherapy source, the residual error is less than 1.2941 mm for all evaluated source positions and less than 0.4141 mm in 75% of positions. This represents a reduction in the error by a factor of 2.4-5.2.

	Residual Error (mm)
Minimum	0.0223
1st quartile	0.1831
Median	0.2818
3rd quartile	0.4141
Maximum	1.2941

Figure 4.7 shows the magnitude of the error as a function of distance from the origin, before and after Compton scatter correction. Post-correction, the error only increases slightly with increasing distance over the range of the treatment volume. Tables 4.1 and 4.2 show the statistics for the residual errors, before and after the Compton scatter correction method is applied; a significant reduction in error is evident (between 2.4 and 5.2, depending on which statistical metric is being considered).

Error statistics after Compton-corrected position estimation for the simulations where the source is located within the nominal FoV are shown in Table 4.2. The median error is less than 0.3 mm, while, the maximum error (due to a small number of outliers) is less than 1.3 mm. This is essentially due to the limited SNR of the 13.5 ms acquisitions of the most distant source locations; the acquired images are quite noisy. At the vast majority (more than 75%) of locations in the quarter-FoV, the post-correction error is less than 0.5 mm. This will be further reduced with longer acquisitions with better SNR, and since the design is intended to operate with an acquisition period of 100 ms, the image SNR should improve by a factor of more than 2.7.

To put the performance of BrachyShade into context, it is useful to consider the magnitude of the various errors associated with HDR brachytherapy source positioning, which was extensively surveyed by Kirisits et al. in 2014 [85]. The largest contributing error is due to swelling of the prostate and surrounding tissues after implantation of the catheters. In the best case, this factor results in an average displacement of the order of ±1.2 mm of the planned position; however, variations of up to 4 mm were observed in some patients [86]. The afterloader also introduces a positioning error, typically of the order of ±1.1 mm. In combination, these errors may easily lead to a real positioning error in excess of 5 mm. Kirisits notes that the implications of this error on the delivered dose are substantial, and lead to average dose uncertainties of around 5% for prostate brachytherapy, with worst-case positioning errors likely leading to much more substantial dose variability. The uncertainties are even higher for cervical brachytherapy.

In this context, the median error in the position estimate provided by BrachyShade of 0.3 mm is sufficiently low that this device will be able to provide a clinically useful estimate of real positioning error.

4.3.2 3 Occluder Probe with Extended FoV

To see the benefits to the FoV of the probe that can be achieved by adding additional occluders, it is first necessary to see the problems which arise if the probe is used to perform source tracking when the source is outside of the primary field of view.

When all points from within the simulation space are used for fitting of the error function in the 3-occluder probe simulations, the overall quality of the fit degrades significantly. This is because for the out-of-primary FoV region (i.e. outside the central wedge), no shadow is visible on the surface of the detector; with little well-defined structure on which to lock, the fitting algorithm does not perform well. Nevertheless, the algorithm does still work to some extent, since some information encoding the source position is still present in the image. As can be seen in Figure 4.8, outside of the central wedge, the error vector field is oriented sharply sideways (in particular, note the lower-right corner of each subfigure).

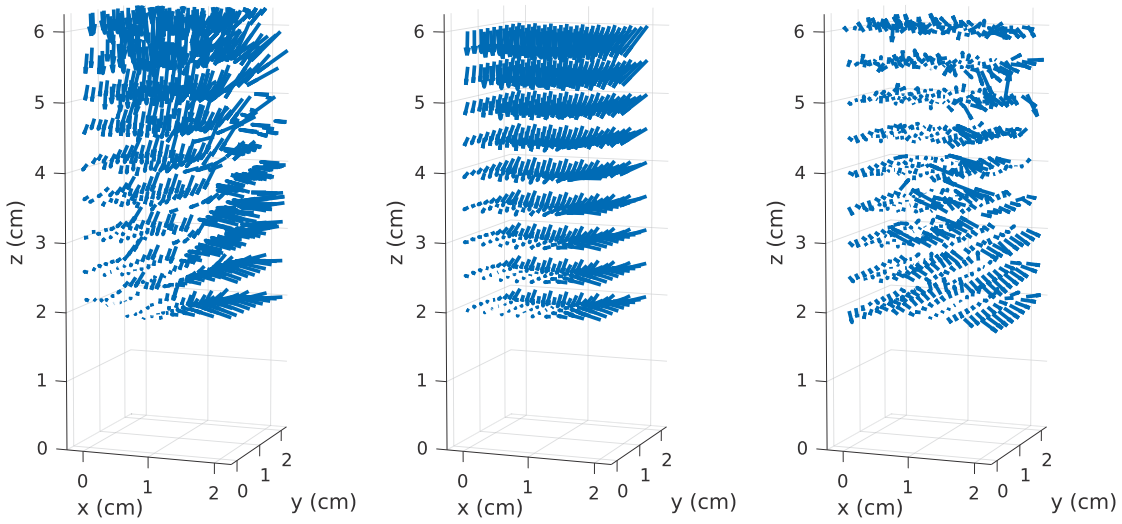

(a) Uncorrected Error Field (b) Correction Field (c) Corrected Error Field

Figure 4.8: Error vector field for 3 occluders as a function of estimated source position; fitted second-order polynomial model of the error vector field; residual error after correction added to original position estimate for the whole FOV.

Table 4.3: Residual error statistics after Compton scatter correction, 3-occluder probe, with all points used to fit the correction coefficients.

	Residual Error (mm)
Minimum	0.0469
1st quartile	0.5210
Median	0.8983
3rd quartile	1.4670
Maximum	5.6285

The resulting correction coefficients are as shown in (4.2), and the post-correction residual error statistics are shown in Table 4.3.

$$\mathbf{A}_x = \begin{bmatrix} -0.1509 \\ 0.1588 \\ -0.0220 \\ 0.0242 \\ 0.0111 \\ -0.0791 \\ 0.0757 \end{bmatrix}; \ \mathbf{A}_y = \begin{bmatrix} -0.0008 \\ 0.0043 \\ -0.0475 \\ 0.0569 \\ -0.0015 \\ 0.0059 \\ -0.0064 \end{bmatrix}; \ \mathbf{A}_z = \begin{bmatrix} 0.0682 \\ -0.1032 \\ -0.0664 \\ 0.0415 \\ -0.0215 \\ 0.0847 \\ -0.0672 \end{bmatrix} \tag{4.2}$$

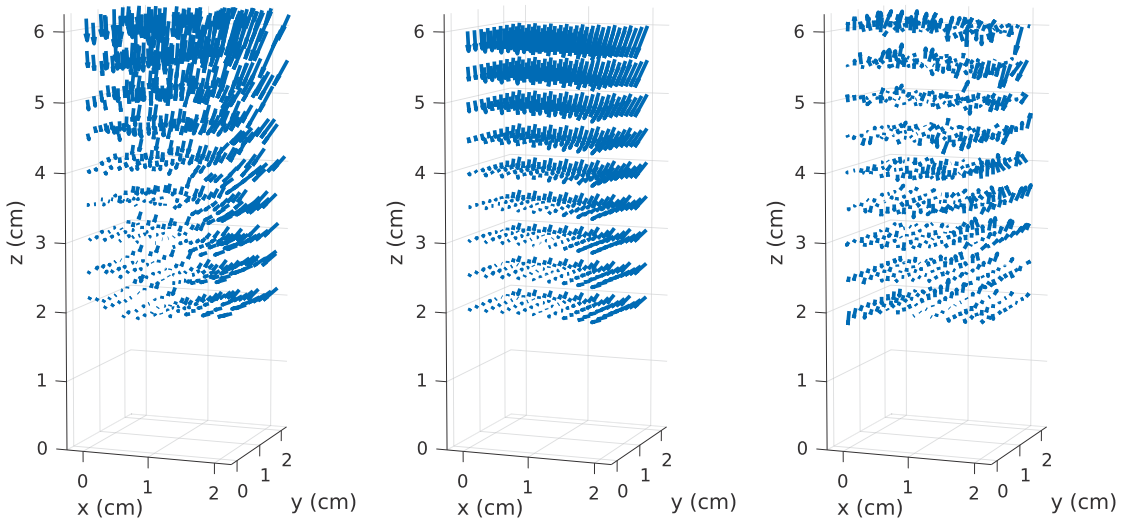

(a) Uncorrected Error Field (b) Correction Field (c) Corrected Error Field

Figure 4.9: Error vector field for 7 occluders as a function of estimated source position; fitted second-order polynomial model of the error vector field; residual error after correction added to original position estimate.

4.3.3 7 Occluder Probe with Extended FoV

By adding an additional pair of occluders to the left and right of the primary three (for a total of seven), the field of view can be significantly increased. Figure 4.9 shows the pre-correction error, correction function and post-correction residual error for the seven-occluder case, with the entire set of 729 points in the quarter-FoV being used to generate the fitting function. The residual error is significantly less biased as a function of position compared to the equivalent extended-FoV evaluation for the 3-occluder probe. Compared to Table 4.3, the residual error observed is reduced by about 1/3. It should be noted that the worst-case error is quite a bit higher than the 3rd quartile value - this is due to the limited SNR of the simulations which have been evaluated leading to a high probability of finding at least one (and possibly more) significant outliers. In practice, with dwell times exceeding 100 ms, SNR will be much better than that shown here, which will significantly reduce the residual error and thus tighten the error statistics.

Table 4.4: Residual error statistics after Compton scatter correction, 7-occluder probe, with all points used to fit the correction coefficients.

	Residual Error (mm)
Minimum	0.0822
1st quartile	0.4484
Median	0.6687
3rd quartile	1.0241
Maximum	4.1444

$$\mathbf{A}_x = \begin{bmatrix} -0.0461 \\ 0.0168 \\ -0.0110 \\ 0.0076 \\ 0.0008 \\ -0.0057 \\ 0.0283 \end{bmatrix}; \ \mathbf{A}_y = \begin{bmatrix} -0.0096 \\ 0.0104 \\ -0.0293 \\ 0.0237 \\ -0.0042 \\ 0.0282 \\ -0.0345 \end{bmatrix}; \ \mathbf{A}_z = \begin{bmatrix} -0.0142 \\ -0.0100 \\ -0.0354 \\ 0.0142 \\ -0.0220 \\ 0.0969 \\ -0.0697 \end{bmatrix} \tag{4.3}$$

4.3.4 Resource requirements and computational complexity

The error-minimisation algorithm works well, and is close to meeting the original design objective of sub-millimetre precision at any evaluated points within the target volume. However, it is computationally expensive, and the time to completion is bounded by the maximum number of iterations and other bail-out criteria as specified in the optimisation algorithm parameters. Typically, 200-300 iterations of the Levenberg-Marquardt algorithm are required to achieve convergence, and no guarantee of globally-optimal solution can be made due to the possibility of becoming trapped in a local minimum. This can be addressed to some degree by repeating the search several times with various pseudorandom permutations of the initial starting point used by the search; however, global optimality still cannot be guaranteed. One possibility is to use the intended location as determined by the treatment planning system as the starting point; the optimisation algorithm should then converge quickly on the true location of the source (which is usually going to be close to the planned location, unless a serious surgical error has occurred. If such a surgical mistake were to occur (which is always a possibility), the algorithm should still prefer to converge to the true location; using

several starting points with random offsets from the planned location and repeating the search would also help to avoid this situation.

Other than computational requirements, the algorithm is very lightweight, and only requires a trivial amount of volatile and non-volatile storage.

4.4 Fast Hierarchical Pattern Matching

4.4.1 Error evaluation at selected points

The second algorithm was tested using the 3-occluder case with a restricted FoV (comparable to the results presented in Section 4.3). The error due to Compton scatter observed with this algorithm is quite different to the error resulting from the (uncorrected) error-minimisation algorithm. A third-order correction term was found to give an optimal post-correction residual error, rather than 2nd order as was used with the other algorithm. The resulting coefficients are listed in (4.4).

$$\mathbf{A}_x = \begin{bmatrix} 0.0779 \\ -0.1011 \\ 0.0897 \\ 0.0208 \\ -0.0591 \\ 0.0374 \\ -0.0059 \\ 0.0642 \\ -0.2038 \\ 0.1719 \end{bmatrix} ; \ \mathbf{A}_y = \begin{bmatrix} -0.0450 \\ 0.1051 \\ -0.0467 \\ -0.2877 \\ 0.8096 \\ -0.4418 \\ -0.0069 \\ 0.0806 \\ -0.2682 \\ 0.2268 \end{bmatrix} ; \ \mathbf{A}_z = \begin{bmatrix} -0.0250 \\ 0.1173 \\ -0.0053 \\ 0.0630 \\ -0.1521 \\ 0.0612 \\ -0.0690 \\ 0.7776 \\ -2.5496 \\ 2.5319 \end{bmatrix} \tag{4.4}$$

A summary of the error statistics is presented in Table 4.5. Overall performance is worse than for the error-minimisation algorithm; however, there are several advantages - chiefly the deterministic time required to obtain the optimal fit, and the ability to guarantee an optimal solution given a sufficiently fine granularity of the search space. It should also be possible to reduce the residual error by further improving the granularity of the fitting library - however, this will come at significantly higher storage costs. However, non-volatile storage and an intelligent caching method can be used to alleviate this problem; these are discussed in Section 4.4.2.

Table 4.5: Residual error statistics after Compton scatter correction with fast hierarchical pattern-matching algorithm; probe is the 3-occluder variant, with all points used to fit the correction coefficients.

	Residual Error (mm)
Minimum	0.1529
1st quartile	0.4475
Median	0.5865
3rd quartile	0.8975
Maximum	0.2540

4.4.2 Resource requirements and computational complexity

While the proposed algorithm is fast, in its current form, it requires substantial memory resources. For example, dividing the 20 mm×20 mm×40 mm volume above the detector into a 64×64×128 point grid, and then storing a 32×128 image for each point, represented as single-point floating point numbers (4 bytes each) requires 64×64×128×32×128×4 bytes, or a total of 8589934592 bytes (2^{33} bytes or 8 GB). However, by only keeping the low-resolution grid in memory, and splitting and storing the high-resolution grid into smaller sub-regions stored in non-volatile memory, the resource requirements are substantially reduced. High-resolution sub-regions can be lazily loaded on-demand and discarded after ageing out (i.e. if a sub-region hasn't been accessed in the last N searches, it can be discarded and re-loaded again if needed.

In terms of computational complexity, the search can be completed in a number of steps approaching $O(\log N)$, where N is the number of points in the search space at the highest resolution. The complexity gets closer to $O(\log N)$ as the number of levels in the hierarchy gets closer to its maximum limit; nevertheless, for practical purposes, two-level hierarchy is sufficient to achieve a search time similar to the error-minimisation algorithm.

4.5 Conclusions

Based on the Monte Carlo simulation results presented in the preceding section, it is clear that Compton scatter correction is absolutely essential to the proper estimation of source position. The proposed method for correcting Compton scatter is very effective, with the residual error in the position estimate now determined principally by the SNR which can be achieved during a given acquisition interval. With the current

simulation results, and with a realistic model of the radioactive source, an error of less than 1.3 mm is achievable even for acquisitions with a much lower SNR than is achievable in practice, while the majority of locations exhibit an error less than 0.5 mm. Performing a larger simulation corresponding to dwell times of 100 ms or more can reasonably be expected to reduce the worst-case error to significantly less than 1 mm.

For the 3-occluder HDR BrachyShade probe, the field of view is limited by the volume above the detector for which a shadow is at least partially projected onto the imaging plane. The addition of further occluders to the left and right of the three occluders modelled in this paper is straightforward, and ensures that a shadow will be projected onto the imaging plane even for much more extreme source positions, essentially extending the field of view to the entire 40 mm $\times$ 40 mm $\times$ 40 mm volume above the probe. This requires no substantial modifications of either the source position estimation algorithm or the Compton scatter correction algorithm; it only marginally increases the execution time for evaluation of the analytic model.

The results presented in this chapter, therefore, demonstrate that the fundamental idea is sound, and that the tracking of a highly radioactive source in a small volume can be achieved with outstanding accuracy and consistency.

CHAPTER 5

Conclusions and Future Work

5.1 Conclusion

A source tracking system was developed which uses shadows cast by tungsten occluders to identify the position of a HDR brachytherapy source in real time. Source tracking with an accuracy of better than 1.3 mm was obtained for a 13.5 ms image acquisition period (for a 370 GBq HDR brachytherapy source) at all source locations within the field of view, with the estimated source position being within 0.5 mm in more than 3/4 of locations within the target volume. The Compton scatter correction algorithm was able to largely correct errors in the estimated source position which result from scattering in the medium.

Chapter 2 presented an extensive literature review, beginning with an introduction to the subject of brachytherapy in general. The importance of and the key principle governing the design of a source tracking system were discussed in detail from an engineering and physics perspective. An extensive review of current quality assurance methods used in HDR prostate brachytherapy has been presented which analysed the limitations of building a source tracking imaging system out-of-body. The review also discussed in details several previous in-body dosimetry, imaging and source tracking systems. The recently-developed HDR BrachyView system was discussed in detail, the probe design and geometry were described and the limitations of this advanced in-body source tracking system were investigated.

The design objectives for a new source tracking system, *BrachyShade*, were introduced in Chapter 3. BrachyShade is inspired by HDR BrachyView, but takes a very different approach to source tracking by tracking the projected shadow of a number of tungsten sphere on an array of four *Timepix* detectors rather than tracking the projected light through the pinholes on the detectors array. Two probe designs with alternative occluder geometries were proposed - one with three occluders, and a second with seven. The key design parameters of BrachyShade, including the characteristics of the detector, the materials and dimensions of the occluders and the plastic tube, the source activity and the field of view were investigated, derived analytically and validated using Geant4 Monte Carlo simulations.

Source position estimation is achieved using an error-minimisation algorithm, which attempts to fit the parameters of an approximate analytical model to the observed photon distribution. An alternative position-based localisation algorithm based on a high-speed template-matching algorithm has also been developed. The algorithms have been implemented using Matlab, and exhaustively evaluated using a prostate brachytherapy QA application as the test case. In this form, the probe is designed for use inside the human body. In-body Compton scattering results in a loss of contrast between the shadowed and unshadowed regions of the acquired image. Therefore, to mitigate the effects of Compton scattering, an empirical model is used to estimate the systemic error that it introduces at any given position in the target volume and correct it. The design of HDR BrachyShade was validated by conducting a series of simulations performed using Geant4 10.3p2. The two alternative designs for the proposed system (i.e. 3-occluder and 7-occluder) were evaluated in terms of sensitivity and accuracy (in terms of residual post-Compton-correction error between the estimated source location and the true location of the source). The results were compared to the performance reported by HDR BrachyView; it is clear that BrachyShade can provide at least as good an estimate of the source position as HDR BrachyView (and potentially better, with sufficient image SNR). The proposed design enables a larger field of view without mechanical rotation of the probe; it is also much easier to accurately manufacture, combining generic components with modern additive manufacturing methods (3D printed polymers).

5.2 Future Work

The next steps planned in the development of the BrachyShade probe over the next twelve months include a detailed simulation evaluation of a 7-occluder variant with increased field of view, performance evaluation with a ^{60}Co source, performance evaluation with simulated 100 ms acquisitions for a range of points within the treatment volume, and fabrication of a prototype (currently in development) for evaluating real-world performance with an actual brachytherapy source.

Bibliography

[1] Australian Institute of Health and Welfare 2017, "Burden of Cancer in Australia: Australian Burden of Disease 2011," Australian Burden of Disease Study series no. 12. Cat. no. BOD 13., AIHW, Canberra, 2017.

[2] O. Lauche, G. Delouya, D. Taussky, C. Menard, D. Béliveau-Nadeau, Y. Hervieux, R. Larouche, and M. Barkati, "Single-fraction high-dose-rate brachytherapy using real-time transrectal ultrasound based planning in combination with external beam radiotherapy for prostate cancer: dosimetrics and early clinical results," *Journal of contemporary brachytherapy*, vol. 8, no. 2, p. 104, 2016.

[3] M. Ahmad, H. Ahmad, M. R. Khattak, K. A. Shah, N. Javed, S. J. A. Shah, W. Shaheen, and K. Mansoor, "Postoperative single versus multiple fractions high-dose rate iridium-192 surface mould brachytherapy for keloid treatment: a comparative study," *Journal of Radiotherapy in Practice*, vol. 17, no. 1, pp. 60–65, 2018.

[4] J. Skowronek, "Brachytherapy in the therapy of prostate cancer–an interesting choice," *Contemprary Oncology (Pozn)*, vol. 17, no. 5, pp. 407–412, 2013.

[5] P. J. Hoskin, K. Motohashi, P. Bownes, L. Bryant, and P. Ostler, "High dose rate brachytherapy in combination with external beam radiotherapy in the radical treatment of prostate cancer: initial results of a randomised phase three trial," *Radiotherapy and Oncology*, vol. 84, no. 2, pp. 114–120, 2007.

[6] G. Gambarini, M. Carrara, C. Tenconi, N. Mantaut, M. Borroni, D. Cutajar, M. Petasecca, I. Fuduli, M. Lerch, E. Pignoli, *et al.*, "Online in vivo dosimetry in high dose rate prostate brchytherapy with moskin detectors: in phantom feasibility study," *Applied Radiation and Isotopes*, vol. 83, pp. 222–226, 2014.

[7] A. N. M. Database, "Cancer mortality trends and projections: 2014 to 2025." http://www.aihw.gov.au/cancer/mortality-trends-projections/, 2017.

[8] R. L. Siegel, K. D. Miller, and A. Jemal, "Cancer statistics, 2015," *CA: A Cancer Journal for Clinicians*, vol. 65, no. 1, pp. 5–29, 2015.

[9] T. A. C. S. medical and editorial content team, "Key statistics for prostate cancer." https://www.cancer.org/cancer/prostate-cancer/about/key-statistics.html, 2017.

[10] C. R. UK, "Prostate cancer statistics." http://www.cancerresearchuk.org/health-professional/cancer-statistics/statistics-by-cancer-type/prostate-cancer?_ga=2.216659542.1555524786.1494556298-2024404577.1494553660, 2017.

[11] T. K. Gupta, *Radiation, Ionization, and Detection in Nuclear Medicine*. Springer, 1st ed., 2013.

[12] S. R. Cherry, J. A. Sorenson, and M. E. Phelps, *Physics in Nuclear Medicine*. Elsevier Health Sciences, 4th ed., 2012.

[13] J. Skowronek, "Low-dose-rate or high-dose-rate brachytherapy in treatment of prostate cancer–between options," *Journal of Contemprary Brachytherapy*, vol. 5, no. 1, pp. 33–41, 2013.

[14] M. Alam, S. Nanda, B. B. Mittal, N. A. Kim, and S. Yoo, "The use of brachytherapy in the treatment of nonmelanoma skin cancer: a review," *Journal of the American Academy of Dermatology*, vol. 65, no. 2, pp. 377–388, 2011.

[15] G. K. Edmundson, F. A. Vicini, P. Y. Chen, C. Mitchell, and A. A. Martinez, "Dosimetric characteristics of the mammosite rts, a new breast brachytherapy applicator," *International Journal of Radiation Oncology* Biology* Physics*, vol. 52, no. 4, pp. 1132–1139, 2002.

[16] J. Skowronek, "Lung cancer brachytherapy," *International Journal of Cancer Research and Prevention*, vol. 4, no. 2, p. 97, 2011.

[17] S. Langley and R. Laing, "Prostate brachytherapy has come of age: a review of the technique and results," *BJU international*, vol. 89, no. 3, pp. 241–249, 2002.

[18] F. Peinemann, U. Grouven, C. Bartel, S. Sauerland, H. Borchers, M. Pinkawa, A. Heidenreich, and S. Lange, "Permanent interstitial low-dose-rate brachytherapy for patients with localised prostate cancer: a systematic review of randomised and nonrandomised controlled clinical trials," *European Urology*, vol. 60, no. 5, pp. 881–893, 2011.

[19] W. C. Kim, G. E. Kim, C. O. Suh, and J. J. Loh, "High versus low dose rate intracavitary irradiation for adenocarcinoma of the uterine cervix," *Japanese Journal of Clinical Oncology*, vol. 31, no. 9, pp. 432–437, 2001.

[20] P. Bownes and A. Flynn, "Prostate brachytherapy: a review of current practice," *Journal of Radiotherapy in Practice*, vol. 4, no. 2-3, pp. 86–101, 2004.

[21] G. Kovács, R. Pötter, T. Loch, J. Hammer, I.-K. Kolkman-Deurloo, J. J. de la Rosette, and H. Bertermann, "Gec/estro-eau recommendations on temporary brachytherapy using stepping sources for localised prostate cancer," *Radiotherapy and Oncology*, vol. 74, no. 2, pp. 137–148, 2005.

[22] S. Strohmaier and G. Zwierzchowski, "Comparison of 60co and 192ir sources in hdr brachytherapy," *Journal of Contemporary Brachytherapy*, vol. 3, no. 4, p. 199, 2011.

[23] M. Barkati, S. G. Williams, F. Foroudi, K. H. Tai, S. Chander, S. van Dyk, A. See, and G. M. Duchesne, "High-dose-rate brachytherapy as a monotherapy for favorable-risk prostate cancer: a Phase II trial," *International Journal of Radiation Oncology Biology Physics*, vol. 82, pp. 1889–1896, Apr. 2012.

[24] L. Jian, W. Zhongmin, C. Kemin, Z. Yunfeng, and H. Gang, "Micropet-ct evaluation of interstitial b rachytherapy in pancreatic carcinoma xenografts," *Acta Radiologica*, vol. 54, no. 7, pp. 800–804, 2013.

[25] C. Kolotas, D. Baltas, and N. Zamboglou, "Ct-based interstitial hdr brachytherapy," *Strahlentherapie und Onkologie*, vol. 175, no. 9, pp. 419–427, 1999.

[26] M. Safavi-Naeini, Z. Han, D. Cutajar, S. Guatelli, M. Petasecca, M. Lerch, D. Franklin, J. Jakubek, S. Pospisil, J. Bucci, *et al.*, "Brachyview, a novel inbody imaging system for hdr prostate brachytherapy: design and monte carlo feasibility study," *Medical Physics*, vol. 40, no. 7, p. 071715, 2013.

[27] M. Safavi-Naeini, Z. Han, S. Alnaghy, D. Cutajar, M. Petasecca, M. L. Lerch, D. R. Franklin, J. Bucci, M. Carrara, M. Zaider, *et al.*, "Brachyview, a novel in-body imaging system for hdr prostate brachytherapy: Experimental evaluation," *Medical Physics*, vol. 42, no. 12, pp. 7098–7107, 2015.

[28] L. Schreiner, I. Crooks, M. Evans, B. Keller, and W. Parker, "Imaging of hdr brachytherapy dose distributions using nmr fricke-gelatin dosimetry," *Magnetic Resonance Imaging*, vol. 12, no. 6, pp. 901–907, 1994.

[29] C. R. King, "Ldr vs. hdr brachytherapy for localized prostate cancer: the view from radiobiological models," *Brachytherapy*, vol. 1, no. 4, pp. 219–226, 2002.

[30] I. S. Grills, A. A. Martinez, M. Hollander, R. Huang, K. Goldman, P. Y. Chen, and G. S. Gustafson, "High dose rate brachytherapy as prostate cancer monotherapy reduces toxicity compared to low dose rate palladium seeds," *The Journal of urology*, vol. 171, no. 3, pp. 1098–1104, 2004.

[31] J. C. Nickel, "Benign prostatic hyperplasia: does prostate size matter?," *Reviews in Urology*, vol. 5 Suppl 4, pp. S12–17, 2003.

[32] P. J. Hoskin, P. J. Bownes, P. Ostler, K. Walker, and L. Bryant, "High dose rate afterloading brachytherapy for prostate cancer: catheter and gland movement between fractions," *Radiotherapy and Oncology*, vol. 68, no. 3, pp. 285–288, 2003.

[33] Z. Han, *Real-time source tracking for quality assurance in HDR prostate brachytherapy*. PhD thesis, University of Wollongong, 2015.

[34] T. Simnor, S. Li, G. Lowe, P. Ostler, L. Bryant, C. Chapman, D. Inchley, and P. J. Hoskin, "Justification for inter-fraction correction of catheter movement in fractionated high dose-rate brachytherapy treatment of prostate cancer," *Radiotherapy and Oncology*, vol. 93, no. 2, pp. 253–258, 2009.

[35] F. L. Cury, M. Duclos, A. Aprikian, H. Patrocinio, and L. Souhami, "Prostate gland edema after single-fraction high-dose rate brachytherapy before external beam radiation therapy," *Brachytherapy*, vol. 9, no. 3, pp. 208–212, 2010.

[36] A. A. Martinez, I. Pataki, G. Edmundson, E. Sebastian, D. Brabbins, and G. Gustafson, "Phase ii prospective study of the use of conformal high-dose-rate brachytherapy as monotherapy for the treatment of favorable stage prostate cancer: a feasibility report," *International Journal of Radiation Oncology* Biology* Physics*, vol. 49, no. 1, pp. 61–69, 2001.

[37] A. M. Dinkla, B. R. Pieters, K. Koedooder, N. van Wieringen, R. van der Laarse, and A. Bel, "Prostate volume and implant configuration during 48 hours of temporary prostate brachytherapy: limited effect of oedema," *Radiation Oncology*, vol. 9, no. 1, p. 272, 2014.

[38] P. Sprawls, *Physical Principles of Medical Imaging*. Medical Physics Publishing Corporation, 2nd ed., 1995.

[39] J. T. Bushberg, J. A. Seibert, and E. M. Leidholdt, *The Essential Physics of Medical Imaging*. Lippincott Williams & Wilkins, 3rd ed., 2011.

[40] G. F. Knoll, *Radiation Detection and Measurement*. John Wiley & Sons, 4th ed., 2010.

[41] D. Schnapauff, T. Denecke, C. Grieser, F. Colletini, D. Seehofer, M. Sinn, J. Banzer, E. Lopez-Hänninen, B. Hamm, P. Wust, *et al.*, "Computed tomography-guided interstitial hdr brachytherapy (ct-hdrbt) of the liver in patients with irresectable intrahepatic cholangiocarcinoma," *Cardiovascular and Interventional Radiology*, vol. 35, no. 3, pp. 581–587, 2012.

[42] W. Zhongmin, L. Yu, L. Fenju, C. Kemin, and H. Gang, "Clinical efficacy of ct-guided iodine-125 seed implantation therapy in patients with advanced pancreatic cancer," *European radiology*, vol. 20, no. 7, pp. 1786–1791, 2010.

[43] M. Carrara, C. Tenconi, D. Mazzeo, A. Romanyukha, M. Borroni, E. Pignoli, D. Cutajar, M. Petasecca, M. Lerch, J. Bucci, *et al.*, "Study of the correlation between rectal wall in vivo dosimetry performed with moskins and implant modification during trus-guided hdr prostate brachytherapy," *Radiation Measurements*, 2017.

[44] M. Waine, C. Rossa, R. Sloboda, N. Usmani, and M. Tavakoli, "Three-dimensional needle shape estimation in trus-guided prostate brachytherapy using 2-d ultrasound images," *IEEE Journal of Biomedical and Health Informatics*, vol. 20, no. 6, pp. 1621–1631, 2016.

[45] M. Schmid, J. M. Crook, D. Batchelar, C. Araujo, D. Petrik, D. Kim, and R. Halperin, "A phantom study to assess accuracy of needle identification in real-time planning of ultrasound-guided high-dose-rate prostate implants," *Brachytherapy*, vol. 12, no. 1, pp. 56–64, 2013.

[46] S. D. Figueroa, C. T. Winkelmann, W. H. Miller, W. A. Volkert, and T. J. Hoffman, "Tld assessment of mouse dosimetry during microct imaging," *Medical Physics*, vol. 35, no. 9, pp. 3866–3874, 2008.

[47] M. Batic, J. Burger, V. Cindro, G. Kramberger, I. Mandic, M. Mikuz, A. Studen, and M. Zavrtanik, "Verification of High Dose Rate ^{192}Ir Source Position During Brachytherapy Treatment Using Silicon Pixel Detectors," *IEEE Transactions on Nuclear Science*, vol. 58, no. 5, pp. 2250–2256, 2011.

[48] J. Lambert, T. Nakano, S. Law, J. Elsey, D. R. McKenzie, and N. Suchowerska, "In vivo dosimeters for hdr brachytherapy: A comparison of a diamond detector, mosfet, tld, and scintillation detector," *Medical Physics*, vol. 34, no. 5, pp. 1759–1765, 2007.

[49] Z. Han, *Real-time source tacking for quality assurance in HDR prostate brachytherapy*. PhD thesis, Faculty of Engineering and Information Scinces, 2015.

[50] B. Reniers, G. Landry, R. Eichner, A. Hallil, and F. Verhaegen, "In vivo dosimetry for gynaecological brachytherapy using a novel position sensitive radiation detector: feasibility study," *Medical Physics*, vol. 39, no. 4, pp. 1925–1935, 2012.

[51] F. Therriault-Proulx, T. M. Briere, F. Mourtada, S. Aubin, S. Beddar, and L. Beaulieu, "A phantom study of an in vivo dosimetry system using plastic scintillation detectors for real-time verification of 192ir hdr brachytherapy," *Medical Physics*, vol. 38, no. 5, pp. 2542–2551, 2011.

[52] T. Nakano, N. Suchowerska, M. Bilek, D. McKenzie, N. Ng, and T. Kron, "High dose-rate brachytherapy source localization: positional resolution using a diamond detector," *Physics in Medicine and Biology*, vol. 48, no. 14, p. 2133, 2003.

[53] Z.-Y. Qi, X.-W. Deng, X.-p. Cao, S.-M. Huang, M. Lerch, and A. Rosenfeld, "A real-time in vivo dosimetric verification method for high-dose rate intracavitary brachytherapy of nasopharyngeal carcinoma," *Medical Physics*, vol. 39, no. 11, pp. 6757–6763, 2012.

[54] E. L. Seymour, S. J. Downes, G. B. Fogarty, M. A. Izard, and P. Metcalfe, "In vivo real-time dosimetric verification in high dose rate prostate brachytherapy," *Medical Physics*, vol. 38, no. 8, pp. 4785–4794, 2011.

[55] G. Gambarini, M. Borroni, S. Grisotto, A. Maucione, A. Cerrotta, C. Fallai, and M. Carrara, "Solid state tl detectors for in vivo dosimetry in brachytherapy," *Applied Radiation and Isotopes*, vol. 71, pp. 48–51, 2012.

[56] L. Wootton, R. Kudchadker, A. Lee, and S. Beddar, "Real-time in vivo rectal wall dosimetry using plastic scintillation detectors for patients with prostate cancer," *Physics in Medicine and Biology*, vol. 59, no. 3, p. 647, 2014.

[57] J. Mason, A. Mamo, B. Al-Qaisieh, A. M. Henry, and P. Bownes, "Real-time in vivo dosimetry in high dose rate prostate brachytherapy," *Radiotherapy and Oncology*, 2016.

[58] L. Cartwright, N. Suchowerska, Y. Yin, J. Lambert, M. Haque, and D. McKenzie, "Dose mapping of the rectal wall during brachytherapy with an array of scintillation dosimeters," *Medical Physics*, vol. 37, no. 5, pp. 2247–2255, 2010.

[59] F. Therriault-Proulx, S. Beddar, and L. Beaulieu, "On the use of a single-fiber multipoint plastic scintillation detector for 192ir high-dose-rate brachytherapy," *Medical Physics*, vol. 40, no. 6, 2013.

[60] J. Duan, D. J. Macey, P. N. Pareek, and I. A. Brezovich, "Real-time monitoring and verification of in vivo high dose rate brachytherapy using a pinhole camera," *Medical Physics*, vol. 28, no. 2, pp. 167–173, 2001.

[61] M. Batič, J. Burger, V. Cindro, G. Kramberger, I. Mandić, M. Mikuž, A. Studen, and M. Zavrtanik, "Localization of high dose rate 192ir source during brachytherapy treatment using silicon detectors," in *World Congress on Medical Physics and Biomedical Engineering, September 7-12, 2009, Munich, Germany*, pp. 577–580, Springer, 2009.

[62] J. Lee, X. Liu, A. K. Jain, J. L. Prince, and G. Fichtinger, "Tomosynthesis-based radioactive seed localization in prostate brachytherapy using modified distance map images," in *2008 5th IEEE International Symposium on Biomedical Imaging: From Nano to Macro*, pp. 680–683, IEEE, 2008.

[63] H. Song, J. Bowsher, S. Das, and F.-F. Yin, "Tracking brachytherapy sources using emission imaging with one flat panel detector," *Medical Physics*, vol. 36, no. 4, pp. 1109–1111, 2009.

[64] R. Wang, J. Ribouton, P. Pittet, P. Guiral, P. Jalade, and G. Lu, "Implementation of gan based real-time source position monitoring in hdr brachytherapy," *Radiation Measurements*, vol. 71, pp. 293–296, 2014.

[65] H. De Leeuw, M. A. Moerland, M. van Vulpen, P. R. Seevinck, and C. J. Bakker, "A dual-plane co-rasor technique for accurate and rapid tracking and position verification of an ir-192 source for single fraction hdr brachytherapy," *Physics in Medicine and Biology*, vol. 58, no. 21, p. 7829, 2013.

[66] P. R. Seevinck, H. de Leeuw, C. Bos, and C. J. Bakker, "Highly localized positive contrast of small paramagnetic objects using 3d center-out radial sampling with off-resonance reception," *Magnetic Resonance in Medicine*, vol. 65, no. 1, pp. 146–156, 2011.

[67] A. Palmer, P. Di Pietro, S. Alobaidli, F. Issa, S. Doran, D. Bradley, and A. Nisbet, "Comparison of methods for the measurement of radiation dose distributions in high dose rate (hdr) brachytherapy: Ge-doped optical fiber, ebt3 gafchromic film, and presage® radiochromic plastic," *Medical Physics*, vol. 40, no. 6, 2013.

[68] A. Sarfehnia, I. Kawrakow, and J. Seuntjens, "Direct measurement of absorbed dose to water in hdr i192r brachytherapy: Water calorimetry, ionization chamber, gafchromic film, and tg-43," *Medical Physics*, vol. 37, no. 4, pp. 1924–1932, 2010.

[69] S.-T. Chiu-Tsao, D. Medich, and J. Munro, "The use of new gafchromic® ebt film for i125 seed dosimetry in solid water® phantom," *Medical Physics*, vol. 35, no. 8, pp. 3787–3799, 2008.

[70] A. L. Palmer, A. Nisbet, and D. Bradley, "Verification of high dose rate brachytherapy dose distributions with ebt3 gafchromic film quality control techniques," *Physics in Medicine and Biology*, vol. 58, no. 3, p. 497, 2013.

[71] A. Micke, D. F. Lewis, and X. Yu, "Multichannel film dosimetry with nonuniformity correction," *Medical physics*, vol. 38, no. 5, pp. 2523–2534, 2011.

[72] D. Granero, J. Perez-Calatayud, and F. Ballester, "Technical note: Dosimetric study of a new Co-60 source used in brachytherapy," *Medical Physics*, vol. 34, pp. 3485–3488, Sept. 2007.

[73] M. Petasecca, K. Loo, M. Safavi-Naeini, Z. Han, P. Metcalfe, S. Meikle, S. Pospisil, J. Jakubek, J. Bucci, M. Zaider, *et al.*, "Brachyview: Proof-of-principle of a novel in-body gamma camera for low dose-rate prostate brachytherapy," *Medical Physics*, vol. 40, no. 4, p. 041709, 2013.

[74] S. Alnaghy, M. Safavi-Naeini, D. R. Franklin, Z. Han, D. L. Cutajar, M. Petasecca, M. Lerch, and A. B. Rosenfeld, "Analytical modelling and simulation of single and double cone pinholes for real-time in-body tracking of an hdr brachytherapy source," *IEEE Transactions on Nuclear Science*, vol. 63, no. 3, pp. 1375–1385, 2016.

[75] V. Kraus, M. Holik, J. Jakubek, M. Kroupa, P. Soukup, and Z. Vykydal, "Fitpix-fast interface for timepix pixel detectors, 2011."

[76] K. Loo, J. Jakubek, J. Zemlicka, M. Petasecca, M. Safavi-Naeini, J. Bucci, M. Zaider, and A. Rosenfeld, "Brachyview: Feasibility study into the application of timepix detectors for soft tissue thickness imaging in prostate brachytherapy treatment," *Radiation Measurements*, vol. 71, pp. 329–332, 2014.

[77] J. Dammer, P. Frallicciardi, J. Jakubek, M. Jakubek, S. Pospisil, E. Prenerova, D. Vavrik, L. Volter, F. Weyda, and R. Zemek, "Real-time in-vivo μ-imaging with medipix2," *Nuclear Instruments and Methods in Physics Research Section A: Accelerators, Spectrometers, Detectors and Associated Equipment*, vol. 607, no. 1, pp. 205–207, 2009.

[78] X. Llopart, R. Ballabriga, M. Campbell, L. Tlustos, and W. Wong, "Timepix, a 65k programmable pixel readout chip for arrival time, energy and/or photon counting measurements," *Nuclear Instruments and Methods in Physics Research Section A: Accelerators, Spectrometers, Detectors and Associated Equipment*, vol. 581, no. 1, pp. 485–494, 2007.

[79] X. Llopart, M. Campbell, R. Dinapoli, D. San Segundo, and E. Pernigotti, "Medipix2: a 64-k pixel readout chip with 55-μm square elements working in single photon counting mode," *IEEE Transactions on Nuclear Science*, vol. 49, no. 5, pp. 2279–2283, 2002.

[80] P. Soukup, J. Jakubek, I. Jandejsek, and J. Zemlicka, "X-ray color imaging with 3d sensitive voxel detector," *Journal of Instrumentation*, vol. 6, no. 12, p. C12014, 2011.

[81] Z. Wang, A. C. Bovik, H. R. Sheikh, and E. P. Simoncelli, "Image quality assessment: from error visibility to structural similarity," *IEEE Transactions on Image Processing*, vol. 13, pp. 600–612, April 2004.

[82] J. Borg and D. W. Rogers, "Spectra and air-kerma strength for encapsulated 192ir sources," *Medical Physics*, vol. 26, no. 11, pp. 2441–2444, 1999.

[83] Z. Han, M. Safavi-Naeini, S. Alnaghy, D. Cutajar, S. Guatelli, M. Petasecca, D. Franklin, A. Malaroda, M. Carrara, J. Bucci, *et al.*, "Radiation dose enhancement at tissue-tungsten interfaces in hdr brachytherapy," *Physics in Medicine and Biology*, vol. 59, no. 21, p. 6659, 2014.

[84] G. M. Daskalov, E. Löffler, and J. F. Williamson, "Monte carlo-aided dosimetry of a new high dose-rate brachytherapy source," *Medical Physics*, vol. 25, no. 11, pp. 2200–2208, 1998.

[85] C. Kirisits, M. J. Rivard, D. Baltas, F. Ballester, M. D. Brabandere, R. van der Laarse, Y. Niatsetski, P. Papagiannis, T. P. Hellebust, J. Perez-Calatayud, K. Tanderup, J. L. Venselaar, and F.-A. Siebert, "Review of clinical brachytherapy uncertainties: Analysis guidelines of GEC-ESTRO and the AAPM," *Radiotherapy and Oncology*, vol. 110, pp. 199–212, jan 2014.

[86] M. Peikari, T. K. Chen, A. Lasso, T. Heffter, G. Fichtinger, and E. C. Burdette, "Characterization of ultrasound elevation beamwidth artifacts for prostate brachytherapy needle insertion," *Medical Physics*, vol. 39, pp. 246–256, dec 2011.